The Astrophysical Journal, 777:66 (16pp), 2013 November 1 doi:10.1088/0004-637X/777/1/66

SHOCK-ENHANCED C^+ EMISSION AND THE DETECTION OF H_2O FROM THE STEPHAN'S QUINTET GROUP-WIDE SHOCK USING *HERSCHEL**

P. N. Appleton[1], P. Guillard[2,3], F. Boulanger[3], M. E. Cluver[4], P. Ogle[5], E. Falgarone[6], G. Pineau des Forêts[3], E. O'Sullivan[7], P.-A. Duc[8], S. Gallagher[9], Y. Gao[10], T. Jarrett[11], I. Konstantopoulos[4], U. Lisenfeld[12], S. Lord[1], N. Lu[1], B. W. Peterson[13], C. Struck[14], E. Sturm[15], R. Tuffs[16], I. Valchanov[17], P. van der Werf[18], and K. C. Xu[1]

[1] NASA Herschel Science Center, California Institute of Technology, Pasadena, CA 91125, USA; apple@ipac.caltech.edu
[2] Spitzer Science Center, California Institute of Technology, Pasadena, CA 91125, USA
[3] Institut d'Astrophysique Spatialé, Universite Paris Sud 11, Orsay, France
[4] Australian Astronomical Observatory, Epping, NSW, Australia
[5] NASA Extragalactic Database, IPAC, California Institute of Technology, Pasadena, CA 91125, USA
[6] Ecole Normale Supérieure/Observatoire de Paris, F-75231 Paris, France
[7] Harvard-Smithsonian Center for Astrophysics, 60 Garden Street, Cambridge, MA 02138, USA
[8] Laboratoire AIM, Saclay, Paris, France
[9] University of Western Ontario, 1151 Richmond Street, London, Ontario, Canada
[10] Purple Mountain Observatory, Nanjing, China
[11] Astronomy Department, University of Cape Town, Private Bag X3, Rondebosch 7701, South Africa
[12] Universidad de Granada, Granada, Spain
[13] University of Wisconsin-Barron County, Rice Lake, WI 54868, USA
[14] Iowa State University, Ames, IA 50011, USA
[15] Max Planck Institute fur Extraterrestische Physik, Munich, Germany
[16] MPI-Kernphysik, Heidelberg, Germany
[17] Herschel Science Center, ESAC, Madrid, Spain
[18] Leiden Observatory, Leiden University, Leiden, The Netherlands

Received 2013 April 3; accepted 2013 September 4; published 2013 October 17

ABSTRACT

We present the first *Herschel* spectroscopic detections of the [O I] 63 μm and [C II] 158 μm fine-structure transitions, and a single para-H_2O line from the 35 × 15 kpc^2 shocked intergalactic filament in Stephan's Quintet. The filament is believed to have been formed when a high-speed intruder to the group collided with a clumpy intergroup gas. Observations with the PACS spectrometer provide evidence for broad (>1000 km s^{-1}) luminous [C II] line profiles, as well as fainter [O I] 63 μm emission. SPIRE FTS observations reveal water emission from the p-H_2O (1_{11}–0_{00}) transition at several positions in the filament, but no other molecular lines. The H_2O line is narrow and may be associated with denser intermediate-velocity gas experiencing the strongest shock-heating. The [C II]/PAH_{tot} and [C II]/FIR ratios are too large to be explained by normal photo-electric heating in photodissociation regions. H II region excitation or X-ray/cosmic-ray heating can also be ruled out. The observations lead to the conclusion that a large fraction the molecular gas is diffuse and warm. We propose that the [C II], [O I], and warm H_2 line emission is powered by a turbulent cascade in which kinetic energy from the galaxy collision with the intergalactic medium is dissipated to small scales and low velocities, via shocks and turbulent eddies. Low-velocity magnetic shocks can help explain both the [C II]/[O I] ratio, and the relatively high [C II]/H_2 ratios observed. The discovery that [C II] emission can be enhanced, in large-scale turbulent regions in collisional environments, has implications for the interpretation of [C II] emission in high-z galaxies.

Key words: galaxies: groups: individual (Stephan's Quintet) – infrared: galaxies

1. INTRODUCTION

The Stephan's Quintet (hereafter SQ) compact galaxy group is unusual among nearby compact groups because it contains a prominent (~35 kpc length) intergalactic filament, first discovered in the radio continuum, but later found to emit optical emission lines and soft X-rays consistent with a large-scale shock (Sulentic et al. 2001; Xu et al. 2003; Trinchieri et al. 2005; O'Sullivan et al. 2009).

The best explanation for the formation of this giant structure is that it represents a region of highly excited shocked gas caused by the collision of a high-speed "intruder" galaxy, NGC 7318b, with a pre-existing tidal filament generated in the past within the group (see discussion by Moles et al. 1998; Sulentic et al. 2001; Williams et al. 2002). Numerical models of the past history of SQ support this picture (Renaud et al. 2010; Hwang et al. 2012; Geng et al. 2012).

The discovery of powerful, $L(H_2) > 10^{42}$ erg s^{-1}, broad (~800 km s^{-1} wide) pure-rotational mid-IR emission lines from warm molecular hydrogen and [Si II] λ34.8 μm (Appleton et al. 2006; Cluver et al. 2010; see Figure 1 (a)) provided the first glimpse of the tremendous dissipation of energy in the shock—the H_2 lines significantly out-shining the soft X-ray luminosity, and optical line emission. The cooling time of the H_2 lines is so short that in-situ heating is required to explain the emission. Guillard et al. (2009) provided an explanation for the similar distribution of warm H_2 and X-ray continuum in terms of the dissipation of energy caused by the collision of the intruder with multi-phase intergroup gas. In this model, X-rays are created in low-density regions which are shock-heated to high temperatures, whereas the H_2 emission arises in denser pockets of gas that survive the passage of the main shock. Additional evidence (Guillard et al. 2012) for a multi-phase shocked medium has come from the discovery of broad-line CO

* *Herschel* is an ESA space observatory with science instruments provided by European-led Principal Investigator consortia and with important participation from NASA.

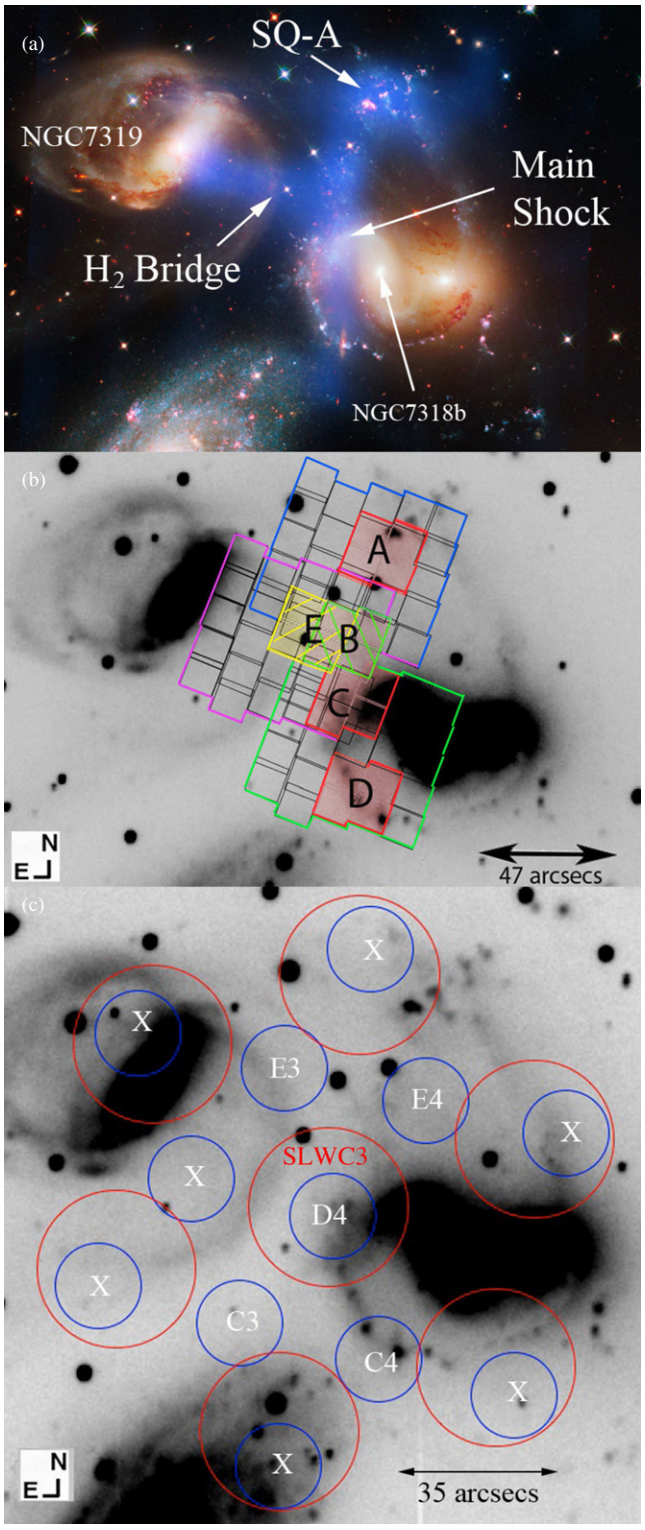

Figure 1. (a) The distribution of warm molecular hydrogen (blue) superimposed on an HSTWFC3 composite color image (red: Hα; green: *V*-band; pale blue: *B*-band) of Stephan's Quintet. The H_2 outlines the 0–0 *S*(1) distribution from Cluver et al. (2010), (b) *R*-band image of Stephan's Quintet showing the outline of the three pointings of the 5 × 5 spaxel PACS IFU (blue, green, and magenta). The lettered regions (A–E) show the extraction boxes discussed in the text. Regions B and E overlap, and were chosen to minimize contamination of the shocked regions by faint star forming emission, (c) SPIRE FTS footprints superimposed on the *R*-band image. Blue and red circles show the SSW and SLW detector beam positions, respectively. Those SSW detectors with letters inside, denote those detectors in which the pH_2O 1_{11}–0_{00} molecule was detected (see Tables 1 and 2). Those with a white "X" show non-detections. SSWC3 was only marginally detected. Upper limits for CO lines at position SLWC3 which is cospatial with SSWD4 are given in Table 2.

(1–0, 2–1 and 3–2) emission from the filament. Molecular gas is seen at velocities ranging from that of the "intruder" galaxy NGC 7318b ($V_{\rm helio}$ = 5774 km s^{-1}) to that of the intergroup gas ($V_{\rm helio}$ = 6600–6700 km s^{-1}). The motions inferred from the CO kinematics support the idea that a significant amount of kinetic energy is still present in the filament. Dissipation of this energy can easily provide a plausible source of in-situ heating of the warm H_2 emission.

Given the potential importance of turbulence and shocks in dissipating mechanical energy throughout the universe, a goal of the current project is to quantify line cooling in an environment which is free of the potentially confusing effects of star formation. If the picture of a turbulent cascade of energy down from the galaxy-collision-scales to the scale of small molecular-clouds is correct, energy may leak out at different scales and densities. Our observations are aimed at quantifying the importance of shocks and turbulence in the main far-IR interstellar medium (ISM) cooling lines of [C II] and [O I]. The SQ filament is an obvious target because we have already seen that molecular line emission is a large fraction of the bolometric luminosity in the structure (Appleton et al. 2006). Furthermore, Suzuki et al. (2011) suggested that [C II] emission might be contributing to a broad-band 160 μm image obtained with *AKARI*. Indeed, the approximate surface brightness levels inferred from their measurements for [C II] contamination are not far from the values we detect spectroscopically in this paper.

In order to address some of these questions, we obtained *Herschel* observations covering the wavelength range of important ISM far-IR emission lines with PACS, as well as SPIRE observations which allow for the potential detection of the higher-*J* transitions of CO (not possible from the ground) which would probe denser and potentially warmer molecular clouds.

Throughout this paper, we adopt a distance to the main background group (excluding the assumed foreground galaxy NGC 7320) of 94 Mpc (Xu et al. 2005). At this distance, 10 arcsec correspond to a linear scale of 4.5 kpc.

2. OBSERVATIONS AND DATA REDUCTION

Observations were made using the PACS integral field spectrometer (Poglitsch et al. 2010) and the SPIRE Fourier Transform Spectrometer (FTS; Griffin et al. 2010) onboard the *Herschel Space Observatory* (Pilbratt et al. 2010) on 2011 December 7–8 and 2012 May 17, respectively, as part of an open time program (PI: Appleton[19]). In addition, *Herschel* photometric observations from a companion paper (P. Guillard et al. 2013, in preparation) will be used to provide far-IR continuum measurements in the current paper.

For the PACS spectrometer, observations of the [C II] 157.74 μm and [O I] 63.18 μm lines were made in the first- and third-order gratings using a short "range-scan" mode covering the redshifted wavelength range 160.4–161.74 and 64.3–64.72 μm, with a velocity resolution of ∼235 and ∼85 km s^{-1}, respectively. The first-order and third-order spectra are detected on independent red and blue spectrometer arrays. The grating was stepped in high sampling mode providing a heliocentric velocity coverage at the [C II] line of 4200–8500 km s^{-1} and 5000–7700 km s^{-1} for [O I] designed to detect broad emission from the group. The PACS integral field unit (IFU) uses an image-slicer and reflective optics to project 5 × 5 spatial pixels (each 9.″4 × 9.″4 on the sky) through the spectrometer system over a total field of view of 47″ × 47″. Three

[19] Program name OT1_pappleto_1.

separate "pointed mode" chop/nod observations were made (3 arcmin chopper throw) with 4 hr of integration time per pointing to cover the main parts of the SQ filament (see Figures 1(a) and (b)). Two of the pointings cover the main north–south structure of the molecular filament, and a third covers a connecting H_2 "bridge" between the main shocked filament and the galaxy NGC 7319 (see Cluver et al. 2010).

PACS data reduction was performed using the standard *Herschel* software Herschel Interactive Processing Environment (HIPE)[20] user build 8.3, and the results were later checked with HIPE 9.0 and 11.1 which have superior flat-fielding capabilities (no significant differences were seen). Data processing included flagging and ignoring bad pixels and saturated data, subtraction of chop "on" and "off" data, division of the relative spectral response function (RSRF), and the application of a flat-field. The data were converted from standard data frames to rebinned data cubes by binning these data in the wavelength domain using default parameters (oversample = 2, upsample = 4) which samples the spectra at the Nyquist rate in the two bands. Finally, data for the two nods were averaged, resulting in a single rebinned data cube for each of the three separate pointing positions (Figure 1(b)).

As a check that the results were not affected by possible uncertainty in the RSRF, and to check that the line fluxes and baselines were the same using both methods (especially in the blue), we also ran these data through a separate pipeline which normalizes the detector signals to an average telescope background spectrum (e.g., see González-Alfonso et al. 2012 for brief description of method)—the so-called flux normalization method.[21] The results were essentially identical both in baseline shape and flux density to less than 5%. For both methods, the primary flux calibration is based on Neptune. Both methods should yield absolute rms flux calibration uncertainties of 11% in both bands.[22]

Because the PACS data were not taken in a fully sampled manner, but rather as three separate pointed observations, we cannot justify extractions of spectra from a combined map. Rather, we choose more correctly, to extract individual spaxels from the cubes. In order to obtain regions significantly larger than the FHWM of the point-spread function (PSF) at both wavelengths (9.3 arcsec at 160 μm and 3.7 arcsec at 64 μm), we generously extracted 2×2 spaxel regions (effectively areas 18.8×18.8 arcsec^2). These five large regions, labeled A through E, were selected for spectral extraction. Since the emission is observed to be quite smoothly distributed on the scale of a few PACS spaxels, the extracted spectra should provide a realistic measurement of the emission in the two lines.

The regions were selected to provide representative samples of the main X-ray and H_2-defined shocked filament which runs nearly north/south over a physical scale of 35 kpc: Regions A–D. Region E, was extracted in the direction of the feature which we call the "H_2 bridge" (see Cluver et al. 2010), which previous observations (Guillard et al. 2012) have shown to contain broad CO lines indicating strong turbulence. In order to ensure we could extract *Spitzer* InfraRed Spectrometer (IRS) spectra from the same regions as PACS, we could not extend our extraction boxes too far to the north or south of the PACS IFU areas without loosing coverage with the IRS short–low module. The short–low module provides crucial information about the strength of polycyclic aromatic hydrocarbon (PAH) features, and proves to be important later in the paper. Region E was chosen specifically to minimize the amount of possible star formation activity in the bridge by inspection of both the 24 μm and 11.3 μm PAH maps of Cluver et al. As a result, Region E has some overlap with Region B. The regions (A–E) were extracted from the final rebinned cubes (slicedFinalCube product) of the level 2 data using the cube analysis task in the Spectrum Explorer package in HIPE 9.1.

SPIRE FTS observations were made in the sparse-mapping single-pointing mode with 100 repetitions. This resulted in 3.7 hr on-source integration time. The SPIRE FTS has two detector arrays, SSW and SLW, covering overlapping bands (194–313 μm and 303–671 μm, respectively), and was used in the high-resolution mode. This provided a spectral resolution $370 < R < 1300$ from the short to longest wavelengths. The FTS data were processed using the HIPE 9.0 user reprocessing script with calibration product spire_cal_9_0. We retained all the inner detectors up to the SSW/SLW co-aligned detector ring. The data were processed to the final level where a point-source spectrum was derived per detector.

Figure 1(c) shows the footprints of the FWHM of individual detector-horn superimposed on the *R*-band image of SQ.

The *Spitzer* IRS observations were made in spectral-mapping mode and cover a large portion of the SQ filament. Full details of these observations have been presented elsewhere (Cluver et al. 2010). IRS data cubes constructed and presented by Cluver et al. were used for comparison with the PACS IFU data as follows. The *Spitzer* SL and LL data cubes, which had been constructed at native spatial and spectral resolution using CUBISM (Smith et al. 2007a), were degraded at each wavelength within the cube to an effective spatial resolution of 9.4 arcsec designed to match the resolution of the *Herschel*-observed [C II] line with PACS (λ observed = 160 μm) using a flux-conserving wavelength-dependant convolution. Spectra extracted from these convolved cubes formed the basis for the comparison between the *Spitzer* and *Herschel* data discussed below.

For the five selected PACS regions, we also extracted photon count and energy information from the deep (95 ks) *Chandra* X-ray map of O'Sullivan et al. (2009). The observations utilized the S3 CCD detector of *Chandra* and the analysis followed the same procedure as described in the above paper, except that the CIAO package (version 4.5 with CALDB 4.5.5.1) was used to extract the PACS target regions. For each region, an absorbed Astrophysics Plasma Emission Code (APEC) model (Smith et al. 2001) was fitted to the regions, providing best-fit values for gas temperature, metallicity, and X-ray luminosity. APEC calculates line and continuum emissivities for hot, optically thin plasma assumed to be in collisional ionized equilibrium, and draws on a library of over a million individual emission lines to build synthetic spectra which are used in the fit.

3. RESULTS

3.1. PACS Spectroscopy: Emission from [C II] and [O I]

The PACS data cubes associated with the three partially overlapping pointings revealed extended [C II] emission over

[20] HIPE is a joint development by the Herschel Science Ground Segment Consortium, consisting of ESA, the NASA Herschel Science Center, and the HIFI, PACS, and SPIRE consortia (Ott 2010).

[21] At the time of writing, the PACS Instrument Control Center recommends that this test be performed as a check of the integrity of the final spectra. Although the shape of the resulting spectra could be affected by different relative normalizations, the absolute calibration should be the same for both methods.

[22] See PACS Spectrometer Calibration Document at http://herschel.esac.esa.int/twiki/bin/view/Public/PacsCalibrationWeb.

most of the region defined by the H_2 filament (e.g., the blue emission in Figure 1(a)). Figures 2(a)–(e) show the extracted spectra from Regions A–E (see Figure 1(b)) for the [C II] 158 μm (solid black) and [O I] 63 μm (solid red) displayed on the same radial velocity scale. To allow a better comparison, the [O I] 63 μm spectra were smoothed to the same velocity resolution as the [C II] spectra (235 km s^{-1}).

The extracted spectra show several unusual features. The [C II] emission is strong, broad, and asymmetric, with typical total line widths exceeding 1000 km s^{-1}. This is consistent with broad warm H_2 emission (Cluver et al. 2010) observed with *Spitzer* with considerably poorer spectral resolution. Fainter emission from [O I] 63 μm is also detected in Regions A, B and C, covering the same velocity range as the [C II]. In D and E, the [O I] seems to be only associated with the lower-velocity component of the [C II] line. We note that the double-peaked profile evident in both the [C II], CO, and [O I] profiles for Region A is very similar to that seen by Williams et al. (2002) with the VLA in H I emission. H I was not detected in the rest of the main north–south H_2 filament of Figure 1, i.e., sampled by Regions B, C, and D, nor in Region E.

The spectra also resemble the single-dish observations of the CO (1–0) transition of the cold molecular gas obtained with the IRAM 30 m telescope by Guillard et al. (2012). Except for Region B, where the IRAM beam is offset from the PACS extraction center by about 14 arcsec (more than half the FWHM of the IRAM beam at 112.8 GHz—the observing frequency of the CO line), the other pointings differ by no more than 4 arcsec. These spectra are shown superimposed on the PACS spectra in Figure 2, and have been smoothed to an effective spectral resolution of 235 km s^{-1} to match the [C II] resolution. Although the [C II] data do not perfectly match the size and shape of the circular IRAM beam (FWHM 22″), the extracted square PACS spaxels in Regions A, B, and C show similar spectral components to the CO. In Regions B and C, a bright low-velocity component and a fainter high-velocity component are evident, whereas for A, the situation is reversed. The [C II] emission seems to fill-in the velocity space between the two main components of the CO emission. The nearest IRAM spectrum to Region E is only offset by 2.6 arcsec in declination from the PACS spectrum and yet shows some differences from the PACS extraction. Recent CO observations made with PdB interferometer (P. Guillard et al., in preparation), show significant velocity gradients across that region in the molecular gas, and so the offset in the IRAM pointing may be responsible for the different line shape between the [C II] and the CO. However, it is clear that both the CO and the [C II] lines are broad there.[23] The overall similarity between the [C II] line profiles, and the CO line profiles in the main part of the filament suggests a kinematic connection between the [C II] emission (and in some cases the [O I] 63 μm emission) and the molecular gas.

In addition to being broad, the [C II] emission is stronger than the [O I] emission (see Table 1 where the extracted line fluxes are presented). We will argue later that this is consistent with a warm diffuse gas heated by a network of low-velocity magnetic shocks (C-shocks) and/or turbulence. The weakness of the [O I] 63 μm emission is not consistent with strongly dissipative J-shocks (Draine et al. 1983; Hollenbach & McKee 1989; Flower & Pineau des Forêts 2012).

[23] Region D in the smoothed IRAM spectrum contains a higher velocity component not seen in the [C II] emission, but this may be partly baseline uncertainty in the IRAM data.

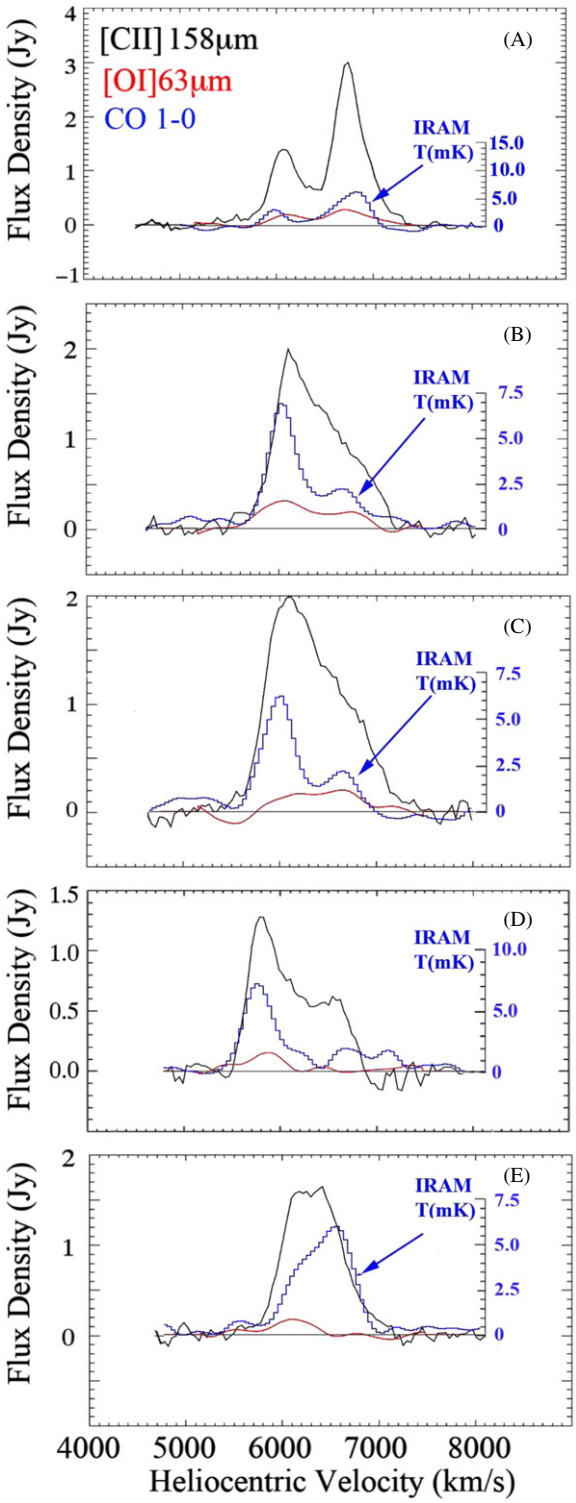

Figure 2. PACS spectra extracted from the five regions shown in Figure 1(b). The black line shows the spectrum of the [C II] line, and the red line the [O I] 63 μm line. Each PACS spectrum represents the sum of the emission over four native spaxels (final area 18.8 × 18.8 arcsec^2). The blue line shows CO 1–0 spectra taken at positions close to the center of the PACS extraction area with the IRAM 30 m telescope from Guillard et al. (2012) with a circular beam size of 22 arcsec diameter. Although the beams are not perfectly matched (Region B is offset by over half the FWHM of the IRAM beam—see the text), it is clear that the CO emission shares a lot in common with the [C II] and [O I] emission. The [O I] and CO data have been smoothed to the same resolution of 235 km s^{-1} as the [C II] line.

Table 1
Line Fluxes of Selected Regions (See Figures 1(b) and (c))

PACS Region[a]	R.A. (J2000)	Decl. (J2000)	$S(1)H_2$ Flux[b]	H_{2tot} Flux[b,c]	$PAH_{(7-8)}$ Flux[b,d]	PAH_{tot} Flux[b,e]	H_{2tot}/PAH_{7-8}	H_{2tot}/PAH_{tot}	H_{2tot}/FIR[e]
A	22 35 58.9	33 58 52.8	3.96 (0.07)	11.44 (0.29)	32.4 (4.4)	59.5 (7.5)	0.35 (0.05)	0.19 (0.02)	0.060 (0.004)
B	22 35 58.9	33 58 29.9	4.39 (0.07)	14.55 (0.28)	6.2 (1.3)	17.38 (4.2)	2.3 (0.5)	0.8 (0.2)	0.132 (0.014)
C	22 35 59.8	33 58 05.3	4.44 (0.07)	17.36 (0.29)	13.3 (3.3)	25.2 (6.1)	1.3 (0.3)	0.69 (0.16)	0.124 (0.012)
D	22 35 59.8	33 57 40.9	2.91 (0.07)	10.54 (0.29)	18.0 (3.3)	31.3 (6.6)	0.59 (0.11)	0.34 (0.07)	0.082 (0.010)
E	22 36 01.6	33 58 25.9	3.86 (0.07)	12.19 (0.29)	2.34 (1.1)	10.44 (3.7)	5.2 (2.5)	1.2 (0.4)	0.106 (0.013)
PACS Region[a]	R.A. (J2000)	Decl. (J2000)	[C II] Line Flux[b]	[O I] 63 μm Flux[b]	[C II]/H_{2tot} Ratio[c]	[C II]/PAH(7.7) Ratio[d]	[C II]/PAH_{tot} Ratio[e]	[C II]/[O I]	[C II]/FIR[f]
A	22 35 58.9	33 58 52.8	9.65 (1.5)	3.9 (0.7)	0.84 (0.13)	0.29 (0.06)	0.16 (0.03)	2.5 (0.77)	0.047 (0.008)
B	22 35 58.9	33 58 29.9	9.02 (1.4)	4.1 (1.0)	0.62 (0.09)	1.45 (0.37)	0.52 (0.15)	2.22 (0.64)	0.078 (0.013)
C	22 35 59.8	33 58 05.3	10.84 (1.6)	2.5 (0.6)	0.62 (0.09)	0.81 (0.24)	0.43 (0.12)	4.34 (1.27)	0.074 (0.012)
D	22 35 59.8	33 57 40.9	5.59 (0.8)	1.2 (0.5)[g]	0.53 (0.08)	0.31 (0.07)	0.18 (0.05)	4.6 (2.0)	0.041 (0.007)
E	22 36 01.6	33 58 25.9	7.34 (1.1)	0.8 (0.4)[g]	0.60 (0.09)	3.1 (1.5)	0.71 (0.27)	9.2 (4.8)	0.061 (0.010)
SPIRE Region[a]	R.A. (J2000)	Decl. (J2000)	p-H_2O 111–000 Flux[b]	S/N	Peak/rms				
SSWD4	22 36 00.4	33 58 04.2	1.24 (0.13)	9.6	4.9	Detected			
SSWE3	22 36 01.2	33 58 36.8	1.25 (0.19)	6.7	3.4	Detected			
SSWE4	22 35 58.7	33 58 29.7	1.44 (0.19)	7.9	4.0	Detected			
SSWC4	22 35 59.6	33 57 32.4	1.06 (0.15)	7.0	3.6	Detected			
SSWC3	22 36 02.0	33 57 40.5	0.73 (0.16)	4.5	2.3	Marginal detection			

Notes.
[a] Regions defined in Figure 1: each covering 18.8 × 18.8 arcsec^2.
[b] Fluxes in units of 10^{-17} W m^{-2}.
[c] Sum over the line luminosities 0–0 $S(0)$ to 0–0 $S(5)$.
[d] Sum over 7.3–8.7 μm PAH complexes.
[e] Sum over 6.3–17 μm PAH bands.
[f] FIR fluxes based on integral over SED (see Table 4 and text).
[g] Marginal detections of [O I].

Table 2
Velocity Components of the Detected [C II], [O I] and H_2O Lines

Name	Line	Ncomps	V_1 (km s^{-1})	δV_1 (km s^{-1})	$Fluxfrac_1$ (percent)	V_2 (km s^{-1})	δV_2 (km s^{-1})	$Fluxfrac_2$ (percent)	V_3 (km s^{-1})	δV_3 (km s^{-1})	$Fluxfrac_3$ (percent)	Comment
A	[C II]	2	6093 (120)	591	30.4	6748 (120)	378	69.6	···	···	···	Poor fit
A	[C II]	3	6101 (80)	383	32	6726 (80)	319	60.0	7024 (80)	234	8	Good
A	[O I] 63 μm	2	6097 (100)	342	35	6719 (100)	512	65	···	···	···	Fair
B	[C II]	3	6121 (80)	415	56	6490 (80)	333	22	6829 (80)	437	22	Good
C	[C II]	2	6041 (80)	475	47	6539 (80)	770	53	···	···	···	Good
D	[C II]	2	5819 (120)	357	50	6377 (120)	637	50	···	···	···	Poor
D	[C II]	3	5781 (80)	281	34	6107 (80)	540	45	6592 (80)	331	21	Good
E	[C II]	2	6078 (80)	234	10	6355 (80)	640	90	···	···	···	Good
SSWD4	p-H_2O ($1_{11}0_{00}$)	1	6457 (120)	<360	100	···	···	···	···	···	···	Sinc function
SSWE3	p-H_2O ($1_{11}0_{00}$)	1	6425 (120)	<360	100	···	···	···	···	···	···	Sinc function
SSWE4	p-H_2O ($1_{11}0_{00}$)	1	6481 (120)	<360	100	···	···	···	···	···	···	Sinc function
SSWC4	p-H_2O ($1_{11}0_{00}$)	1	6380 (120)	<360	100	···	···	···	···	···	···	Sinc function
SSWC3	p-H_2O ($1_{11}0_{00}$)	1	6353 (120)	<360	100	···	···	···	···	···	···	Marg. detection

Single and multiple Gaussian line fitting of the extracted [C II] (and [O I] where appropriate) was performed using the ISAP package developed for *Infrared Space Observatory* (*ISO*; Sturm et al. 1998). Line fluxes for the decomposed Gaussian fits are given in Table 2. Regions B, C, and D required three different velocity components spanning the range from 6000–7000 km s^{-1} to provide a good fit to these data—in most cases very large line widths were required. Region C and E have the broadest fitted single components with FWHM of 630 and 750 km s^{-1}, respectively, although the composite spectra span over 1000 km s^{-1} in total dispersion.

3.2. The SPIRE Spectra

At each detector position, we simultaneously fit a polynomial continuum and all the targeted lines with individual SINC profiles in frequency. For each SINC profile, we initially fixed the FWHM at the value for an unresolved line (1.44 GHz). The targeted lines are the CO rotational transitions, known water lines, [N II] 205 μm, [C I] 370, and 609 μm. The only clearly detected line is the water line p-H_2O ($1_{11}0_{00}$) at ν_{rest} 1113.3 GHz (= 269.28 μm), which is detected S/N > 5 in four SSW detectors: SSWD4, SSWE3, SSWE4, and SSWC4.

Table 3
Upper Limits to Important Undetected Lines

SPIRE Detector[a]	Line	Rest ν (GHz)	R.A. (J2000)	Decl. (J2000)	Line Flux[b]	Beam FWHM (arcsec)	Comment
SLWC3	CO 4–3	461.040	22 36 00	33 58 04	<1.1	46	3σ upper limit
SLWC3	CO 5–4	576.267	22 36 00	33 58 04	<0.46	37	3σ upper limit
SLWC3	CO 6–5	691.473	22 35 00	33 58 04	<0.27	31	3σ upper limit
SLWC3	CO 7–6	806.651	22 35 00	33 58 04	<0.21	26	3σ upper limit
SLWC3	CO 8–7	921.800	22 35 00	33 58 04	<0.34	23	3σ upper limit
SLWC3	pH_2O $2_{02}1_{11}$	987.927	22 35 00	33 58 04	<0.48	21	3σ upper limit
SLWC3	pH_2O $2_{11}2_{02}$	752.033	22 35 00	33 58 04	<0.26	28	3σ upper limit
SLWC3	o$H_2O1_{10}1_{01}$	556.936	22 35 00	33 58 04	<0.47	38	3σ upper limit
SSWD4	[N II] 205 μm	1461.132	22 35 00.4	33 58 04.2	<0.27	14	3σ upper limit
SSWD4	OH^+_c	1033.004[c]	22 35 00.4	33 58 04.2	<0.45	21	3σ upper limit
SLWC3	OH^+_a	909.045[c]	22 35 00.4	33 58 04.2	<0.30	23	3σ upper limit
SLWC3	OH^+_b	971.803[c]	22 35 00.4	33 58 04.2	<0.28	22	3σ upper limit

Notes.
[a] Regions defined in Figure 1.
[b] Fluxes in units of 10^{-17} W m^{-2}.
[c] OH^+ rest frequencies from Bekooy et al. (1985).

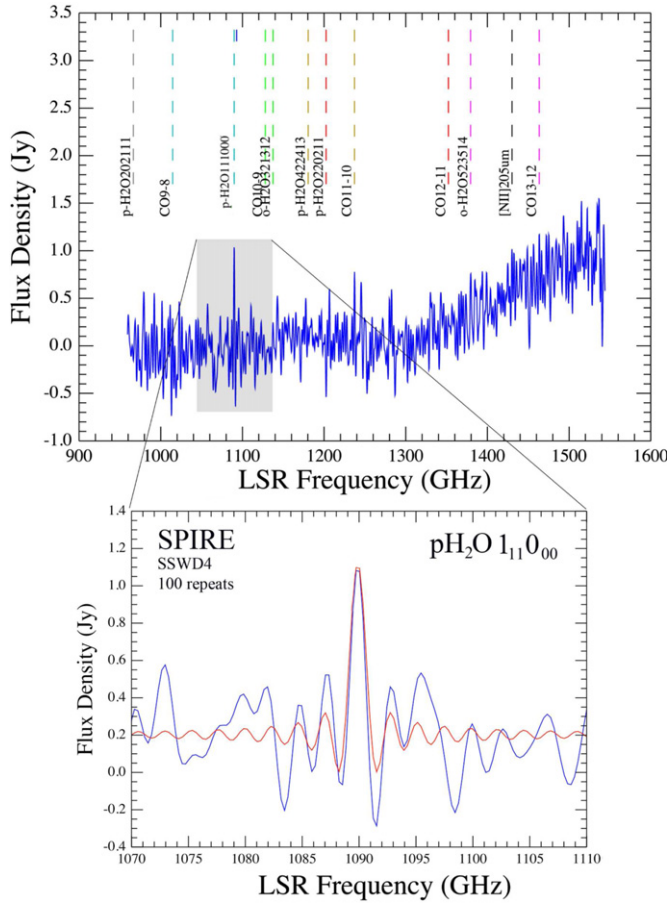

Figure 3. SPIRE FTS spectrum at position SSWD4 (see Figure 1(c)) covering the range 900–1600 GHz and the detection of the pH_2O line. Note the lack of detection of the [N II] 205 μm line at 1461 GHz. The zoomed inset shows a fit to the line with a SINC function (red line).

The SSW spectrum for detector D4 is shown in Figure 3, where the zoomed-in region shows the p-H_2O ($1_{11}0_{00}$) line, detected at a S/N of ~10 (see Table 1). We refitted this line allowing the FWHM to vary, but the line was still found to be unresolved at 324 km s^{-1} (1.44 GHz) resolution. This is in strong contrast to the [C II] and [O I] emission which appears much broader. The SPIRE fitted heliocentric velocities and FWHM for the detected positions are provided in Table 2. The heliocentric radial velocity of the H_2O line for SSW D4 is 6457 ± 120 km s^{-1}, which places it close to the line-center of the broad, but asymmetric [C II] emission from the same position (PACS Region C of Figure 2(c)). Table 2 also provides the central velocity and FWHM for the other detections in SSW E3, E4, and C4. Note that there appears to be a significant radial velocity difference between the center of the SQ shock near SSW D4 and the SSW C4 (shock-south) and SSW E3 (shock-north) detector positions. This follows the general trend of lower heliocentric velocities in the southern part of the shocked filament (Guillard et al. 2012).

Interestingly, no other H_2O lines are detected (Table 3 provides upper limits). On the para-H_2O ladder, the next highest ground-state transition is the p-H_2O (2_{02} 1_{11}) line at 987 GHz, and on the otho-ladder, the o-H_2O (1_{10} 1_{01}) at 557 GHz. Neither of these or other higher-order lines are detected at 3σ levels of <0.48–0.2 × 10^{-17} W m^{-2}, 3–5 times lower than the detection of the pH_2O (1_{11} 0_{00}) line.

The [N II] λ205 μm line (ν_{rest} = 1461.13 GHz), a line often associated with H II regions, is not detected, nor are any of the higher-J CO lines, commonly found in SPIRE spectra of higher-excitation galaxies detected convincingly. Upper limits for these and other commonly encountered ISM lines are also given in Table 3.

3.3. Comparisons with the Spitzer IRS: Extraction of H_2 and PAH Features

Spitzer IRS observations obtained as part of a large spectral mapping program (Cluver et al. 2010) contain important spatial information about molecular hydrogen cooling and PAH emission across the SQ filament. For comparison with the PACS regions, we performed matching extractions of the IRS data cubes covering the same areas as the PACS Regions A–E. The spectra, shown in Figure 4, are strongly dominated by molecular hydrogen lines.

Figure 4 also shows the model result of running PAHFIT (Smith et al. 2007b) on the spectra. The red lines show the fits to atomic and molecular lines (mainly H_2), and the green line

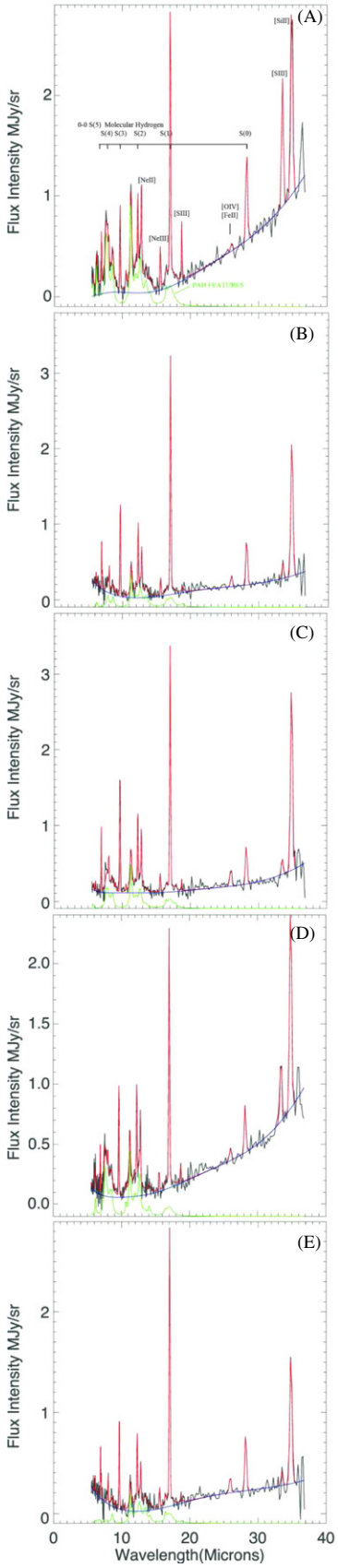

Figure 4. *Spitzer* IRS data taken from spectra cubes of the SQ shock regions discussed in Cluver et al. (2010). The five spectra were extracted from the data cube over the same area as the spaxels which contribute to the five spectra shown in Figure 2. Note the very strong pure rotational H_2 lines, and weak PAH features (shown in green) based on the model fit from PAHFIT. The blue line represents the continuum fitted simultaneously with the lines and bands.

under each spectrum shows the fitted PAH features. The results of the fit, converted into line fluxes, are presented in Table 1. It is clear from the spectra that the H_2 lines, 0–0 $S(0)$ to $S(5)$, dominate the spectrum of the SQ filament, with faint emission from [Ne II] 12.8 μm. Stronger emission from the [Si II] 34.8 μm line is likely shock-excited (Cluver et al. 2010).

The IRS spectra in Figure 4 show that in the filament, the 6.3 and 7.7 μm PAH bands, usually associated with star formation are very weak, especially in PACS Regions B, C, and E. Faint 11.3 μm PAH is detected at most positions, although the total power in all of the PAH lines is small. In Table 1, we tabulate the power in the 7–8 μm PAH features (defined as the sum of the 7.4, 7.6, 7.8, 8.3, and 8.6 μm bands if present), as well as the integral over the main PAH bands (PAH_{tot} defined here as the sum of all the common PAH features from 6.3–17 μm). We find ratios of $0.35 < H_{2tot}/PAH_{7-8} < 5.2$, and $0.19 < H_{2tot}/PAH_{tot} < 1.2$, values that are incompatible with photodissociation region (PDR) photoelectric heating efficiencies and observations of normal galaxies (see Section 5.3). This property, and the absence of a strong enough soft X-ray flux led to the conclusion that the warm H_2 detected by *Spitzer* must be shock excited (see also Guillard et al. 2009). The values with the lowest H_2/PAH ratios are Regions A and D, both of which are known to contain some star formation. Here, some PDR heating of the gas may be present, but not dominant.

Unusually large H_2/PAH ratios are also found in the turbulent bridge region between the Taffy galaxies (Peterson et al. 2012), and in a subset of radio galaxies where shock-excitation is believed to heat the H_2 to several hundred K (Ogle et al. 2010; Guillard et al. 2012), as well as in a subset of active galactic nucleus (AGN) dominated galaxies in the SINGS survey (Roussel et al. 2007).

Later in the paper, we will compare the far-IR spectra with the mid-IR spectral properties from these IRS extractions.

3.4. Comparison with Far-IR Continuum Emission from Spitzer and Herschel Imaging

Observations of the IR continuum observations in SQ have been hampered by poor spatial resolution at the longer wavelengths with *ISO* and *Spitzer* (Xu et al. 2003; Cluver et al. 2010; Natale et al. 2010; Guillard et al. 2010). New PACS and SPIRE observations have recently been made (P. Guillard et al. 2013, in preparation), and we borrow some of the results from that paper to compare with the spectral line properties. Photometry was extracted from archival *Spitzer* 24 μm (Cluver et al. 2010), and the new observations in the PACS 100 and 160 μm and SPIRE 250, 350, and 500 μm bands. A full description of the photometric *Herschel* observations is given in the companion paper of P. Guillard et al. 2013, in preparation).

In order to gain the best possible measurement of the mid- to far-IR luminosity from the PACS spectroscopic extraction regions, we followed a two-step process. First we convolved the 24, 100, 160, 250, and 350 μm maps to a spatial resolution appropriate for the 500 μm SPIRE image ($\sim$29 arcsec FHWM). We then extracted a spectral energy distribution (SED) at these five wavelengths from each of the Regions A–E shown in Figure 1(b). This allowed us to fit the 24–500 μm SED with a modified black-body and a mid-infrared power-law (see Casey et al. 2012 for a description of the method). We computed the gas masses from the dust masses, assuming a dust-to-gas mass ratio of 0.006 (Xu et al. 2003). We call this the "smoothed" SED model.

Table 4
Far-IR SED Fitted Properties for PACS Regions[a]

PACS Region[b]	α[c]	T_{dust} (K)	FIR Flux[d,e] (42–122 μm)[f]	Log(L_{FIR})[g] (10^{35} W)	$\nu F_{70}/\nu F_{100}$	LOG(M_{dust}) ($M_\odot$)	LOG(M_{gas}) ($M_\odot$)
A	1.9 (0.1)	22.9 (0.5)	1.92 (0.13)	2.02 (0.13)	0.55 (0.05)	6.02 (0.06)	8.24 (0.09)
B	2.1 (0.1)	22.7 (0.7)	1.10 (0.12)	1.16 (0.13)	0.52 (0.05)	5.82 (0.08)	8.04 (0.10)
C	2.1 (0.1)	23.7 (0.6)	1.40 (0.14)	1.47 (0.14)	0.53 (0.05)	5.83 (0.07)	8.05 (0.01)
D	2.0 (0.1)	24.0 (0.8)	1.29 (0.15)	1.36 (0.15)	0.55 (0.05)	5.76 (0.08)	8.05 (0.11)
E	1.5 (0.1)	21.8(0.8)	1.15 (0.14)	1.21 (0.14)	0.63 (0.06)	5.82 (0.08)	8.05 (0.01)

Notes.
[a] Using the SED fitting method of Casey (2012).
[b] PACS Regions as defined in Figure 1(b) and Table 1 covering 18.8 × 18.8 arcsec^2.
[c] Parameters from Casey (2012). Dust properties assume a dust emissivity of the form $\nu^{1.8}$, and power law index α.
[d] Derived from *Herschel* photometry observations described in companion paper—P. Guillard et al. 2013, in preparation.
[e] Fluxes in units of 10^{-15} W m^{-2}.
[f] See Dale & Helou (2002).
[g] Assuming $D = 94$ Mpc.

Secondly, in order to estimate the far-IR (FIR) fluxes (Helou et al. 1985; Dale & Helou 2002) in each region, on an angular scale comparable with the [C II] data, we re-extracted the 160 μm fluxes at the full resolution of the 160 μm map. We then normalized the smoothed SED model to the value at 160 μm from the full-resolution map to derive FIR flux per aperture over the range 42–122 μm. Figure 5 shows the SED obtained from the smoothed data, as well as the SED after tying it to the full resolution 160 μm data, for two examples, Regions A and E. The effect of scaling the SED results in only a minor change when the dust emission is extended (as in the case of Region E). The low flux value for the 24 μm point in Region E, when scaled to the resolution of the 160 μm observation (red point), is evidence for a dearth of small grains (see later). The FIR properties measured in each of the five PACS apertures calculated by this method are given in Table 4.

Based on the FIR fluxes and [C II] line strength (summed over all the velocity components detected within each PACS aperture), we calculate the [C II]/FIR ratio, and this is given Table 1. It can be seen that these ratios are unusually large, ranging from ∼0.04 (Regions A and D) to 0.06–0.08 (Regions B, C, and E). In general, [C II]/FIR ratios of less than 1% are common in normal galaxies (see Figure 8). Interestingly, the regions that have the highest [C II]/FIR ratios are also the same regions that show the most extreme [C II]/PAH ratios. Those regions with known star formation (Regions A and D) have lower ratios, indicating that the star formation influences the results by lowering both ratios.

We also approximately measure the intensity ratio of the [C II] to CO (J = 1–0) transition based on the spectra of Figure 2, given that the extraction regions for the [C II] are square and not always precisely aligned with the IRAM 30 m beam. The CO spectra were converted to Jansky units from antenna temperature assuming a value of 6.2 Jy K^{-1}, a value appropriate for compact emission smaller than the 22 arcsec beam. We also scaled the [C II] extracted fluxes by a factor of 1.54 to account for the difference in the areas of the [C II] and CO extractions. If the emission is clumpy on the arcsec scale, this scaling may not be appropriate, and the [C II]/CO ratio would be lower. The results range from $1000 < I([\mathrm{C\,II}])/I(\mathrm{CO}\ J = 1\text{–}0) < 1700$ in Regions B–E, and 2400 in Region A (which includes emission from the SQ-A star forming region). These values are on the low-end of the distribution of values found in the Milky Way and other nearby galaxies (e.g., Stacey et al. 1991, 2010). One

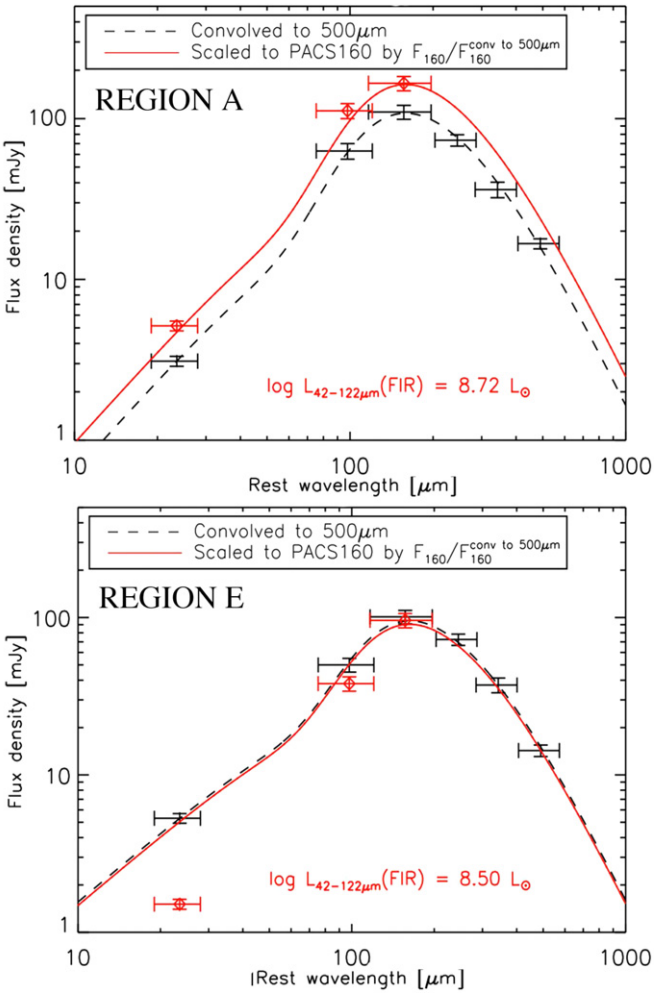

Figure 5. Example far-IR SEDs PACS Regions A and E discussed in more detail by P. Guillard et al. 2013, in preparation). The black data points represent extracted fluxes from 24, 100, 160, 250, and 350 μm *Spitzer*, PACS, and SPIRE images smoothed to the resolution of the SPIRE 500 μm map. The black dotted line represents a fit (using the method of Casey 2012; see also Table 4) to this is called "smoothed model" fit. The red data points represent the measured fluxes 24, 100, and 160 μm *Spitzer* and *Herschel* PACS images (24 and 100 μm smoothed to the resolution at 160 μm). The red curve is the black-dotted line scaled to the flux at full resolution PACS 160 μm band to provide an estimate of FIR luminosity at the same spatial resolution as the [C II] line (see text). For Region A, the flux increased in the full resolution SED because the emission is more point-like there.

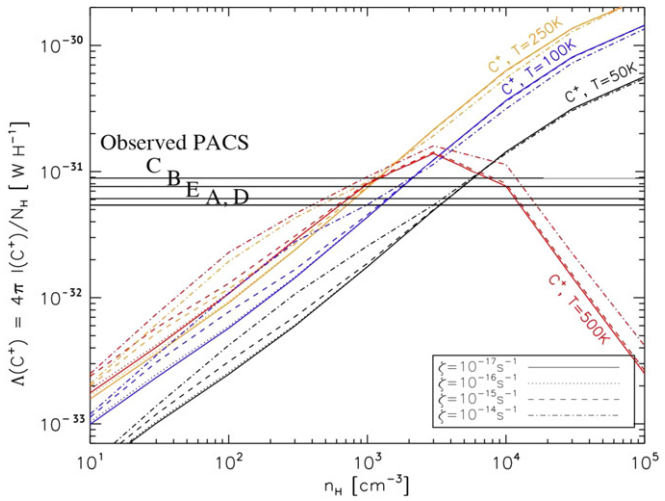

Figure 6. Theoretical models of the C^+ cooling rate as a function gas density and temperature for various values of an assumed temperature and cosmic-ray ionization rate (see the text). Horizontal lines show the measured cooling rate of the C^+ observed by PACS for an assumed gas mass derived from the dust SED and an assumed gas to dust ratio of 0.006 (Xu et al. 2003).

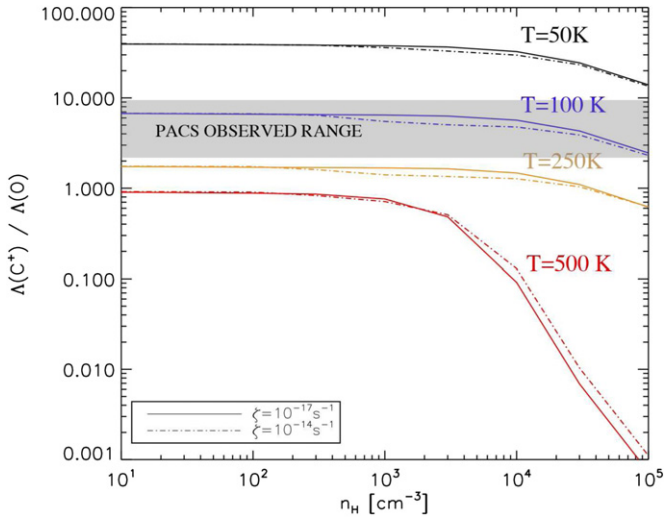

Figure 7. Models of the C^+/oxygen cooling rate ratio as a function gas density and temperature for various values of the assumed cosmic-ray ionization rate (see text). Horizontal gray bar denotes the observed range in the ratio [C II]/[O I] 63 μm (Table 1) for each of the PACS extraction regions. The upper bound is Region E which has a large uncertainty. The 63 μm line dominates oxygen cooling.

might be tempted to conclude that the low values of the I([C II])/I(CO) ratio point toward a low-excitation PDR model, but this is not the case because the same regions also have very elevated [C II]/FIR ratios placing them outside of any standard PDR model (see Stacey et al. 2010; Figure 3). Low metallicity is also unlikely to be the explanation. The *average* metallicity of the gas (summed over all the velocity components) is either mildly sub-solar or approximately solar (see Section 5.3 for a more complete discussion). Furthermore, our observations of the I([C II])/I(CO) ratio deviate significantly (to *lower* values) from those measured in the LMC/SMC. We will show later that shock models are capable of reproducing the observed ratios.

4. EVIDENCE FOR DIFFUSE, WARM MOLECULAR GAS FROM [C II] AND [O I] COOLING RATES

To constrain the gas temperature and density, we computed the theoretical C^+ and oxygen cooling rates with a simple numerical model to compare with our observations. This code computes the gas chemistry and thermal balance at a constant temperature and density, assuming the carbon is all in the form of C^+. It makes no a priori assumptions about the source of heating which we will consider in the next section. We considered 42 chemical species use a chemical network of 285 reactions (a simplified version of the one used in the shock model of Flower et al. 2003), and assume solar metallicity. For the [C II] and total oxygen cooling rates, we consider the collisional effect of primarily H and H_2. We also include cosmic-ray (CR) heating, and parameterize its influence via the CR ionization rate. The results of those calculations for several different temperatures, densities, and CR ionization rates are shown in Figures 6 and 7. Figure 6 shows the [C II] cooling rate as a function of gas density for four different temperatures and several CR ionization rates. The figure shows that at $n_H > 10^3$ cm^{-3}, the [C II] cooling rate does not depend strongly on the CR ionization rate, because the gas rapidly recombines at higher densities. Above $T \sim 500$ K, the [C II] cooling drops at high densities where oxygen cooling dominates. Horizontal lines denote the observed line cooling in the five PACS Regions A–E, as discussed below.

Figure 7 shows the model ratio of the C^+ to total oxygen cooling (both the [O I] 63 and 145 μm lines) as a similar function of density and temperature. Although the model does not distinguish between the two oxygen lines, [O I] 63 μm emission is the dominant coolant over the range of densities and temperatures considered here.

How do these models compare with the observations of the [C II] lines? The [C II] cooling rates for the five regions observed with PACS are computed as $\Lambda(C^+) = L(\mathrm{C\,II}) \times m_H/M_{gas}$, where m_H is the hydrogen mass and M_{gas} is the mass of C II-emitting gas. Let us first assume that the total gas mass can be derived from the far-IR observations (P. Guillard et al. 2013, in preparation) based on an assumed dust-to-gas ratio of 0.006 (e.g., from Xu et al. 2003). These values are provided in Table 4 for each PACS region, and lie in the narrow range $9.5 \times 10^7 < M_{gas}/M_\odot < 1.7 \times 10^8$, and a dust temperature of 22–24 K. If we assume that all of this gas mass is involved in the observed [C II] cooling, then the cooling rates, based on each PACS region will range from 5–9 $\times 10^{-32}$ W H-atom^{-1} shown by the horizontal lines in Figure 6. The comparison of the modeled and observed cooling rates shows that with this relatively high gas mass, the models, and observation constrain the gas to be relatively warm ($50 < T < 500$ K) and of moderate density ($500 < n_H < 3$–7×10^3).

The temperature can be further constrained if we also include the observed [O I] 63 μm line cooling, and the ratio of the [C II]/[O I] 63 μm obtained from Table 1 (ranging between values of 2 and 9) and shown in Figure 7. This indicates that the temperature of the gas lies in an approximate range of $90 < T < 200$ K. Combining the two diagnostics of Figures 6 and 7, we can conclude that if all the gas inferred from the dust SED takes part in the atomic line cooling, then the gas density lies in a narrow range of densities around 10^3 cm^{-3} and a temperature of between 90 and 200 K.

It may be no coincidence that this temperature is similar to the dominant temperature found by analysis of the warm H_2 gas observed by *Spitzer* (see Cluver et al. 2010). For example, one could imagine that the warm H_2 mass detected from *Spitzer* might be the dominant collisional heating source for the [C II] emission. To consider this possibility, we derive the associated warm molecular hydrogen mass for each of the PACS extraction regions based on a simple two-temperature fit to the

Table 5
H_2 Properties Derived from *Spitzer* IRS Observation for Each PACS Region[a]

PACS Region[a]	N1(H_2) $\times(10^{19}$ cm^{-2})	T1 H_2 K	OPR[b]	M1$_{H2}$ $M_\odot$ ($\times10^7$)	N2(H_2) $\times(10^{17}$ cm^{-2})	T2 H_2 K	OPR	M2$_{H2}$ $M_\odot$ ($\times10^5$)
A	14.0	157	2.6	15.2	6.6	628	3	7.1
B	5.9	187	2.8	6.3	7.4	666	3	8.0
C	4.0	201	2.9	4.3	8.8	676	3	9.5
D	2.0	217	2.9	2.2	6.9	617	3	7.4
E	6.7	175	2.7	7.2	5.9	663	3	6.3

Notes.
[a] PACS regions as defined in Figure 1(b) and Table 1 each covering 18.8 × 18.8 arcsec^2.
[b] Ortho to para ratio determined from the fit to the H_2 excitation diagrams for each position.

excitation diagrams of each region derived from the *Spitzer* spectral extractions. These warm H_2 masses are presented in Table 5. These masses are only a factor of two smaller than the gas masses estimated from the dust SED, ranging from 4–7 × 10^7 $M_\odot$ for PACS Regions B, C, and E.[24]

Under the assumption that the C^+ gas is primarily collisionally heated by the warm H_2, the cooling rate per H-atom (horizontal lines in Figure 6) would double, leading to solutions with densities $1.5 \times 10^3 < \rho < 4 \times 10^3$ cm^{-3}. The general conclusion of the study of the cooling rates of the far-IR lines is that the gas in the filament is both warm and diffuse. It is thus very plausible that the warm H_2 and the [C II] and [O I] emitting gas are well mixed in approximate thermal balance.

5. POSSIBLE HEATING SOURCES FOR THE [C II]-EMITTING GAS

We have shown in the previous section that the [C II] emission is consistent with heating by a warm diffuse gas. What would be the source of heat for this gas?

5.1. Extended Distributions of H II Regions?

Could the [C II] emission we observe be the result of collisional excitation of the ground-state C+ ions by hot electrons in the plasma associated with a faint population of H II-region population scattered throughout the filament? Although there is evidence for a sparsely scattered population of H II regions in the shock based on optical and mid-IR measurements (Appleton et al. 2006; Cluver et al. 2010; Guillard et al. 2010), we can directly rule this out from our own observations. Firstly, our SPIRE observations, which cover similar regions to those observed by PACS, show no detection of the [N II] 205 μm nebula line down to a 3σ uncertainty of 2.7×10^{-18} W m^{-2} for detector SSW D4 (centered close to Region C) and 2.0×10^{-18} W m^{-2} for the average flux over the four inner detectors which were seen to show H_2O emission. The [N II] 205 line, because its ionization potential is 14.53 eV (Oberst et al. 2006), almost always arises in H II regions. The lower limit to the ratio of [C II] to [N II], after making a minor renormalization for the area of the SPIRE beams to that of PACS extraction area, is $I(C^+)/I([N\,II]\,205) > 36$ for Region C. These values are significantly higher than those expected for diffuse ionized emission over a realistic range of densities by a factor of >7.

This is not a surprise, since it has been known for some time that the SQ filament contains only a scattering of compact H II regions along its length (see Xu et al. 2003; Oberst et al. 2006; Trancho et al. 2012). These H II regions occupy a small volume of the filament. Furthermore, the mass of gas required to explain the strength of the [C II] line is far too large to be associated with the observed compact H II regions. Guillard et al. (2009) estimated the mass of ionized gas to be 1.2×10^6 $M_\odot$ over an aperture of 5.2 × 2.1 kpc^2, based on the emission measure of the Hα line obtained across the filament by Xu et al. (2003), and assuming reasonable conditions in the diffuse medium for the post-shocked gas. This is at least an order of magnitude below the total warm molecular mass in the same aperture.

5.2. X-Ray Heating?

Given that the SQ filament is known to emit soft X-rays, it is reasonable to ask whether X-rays could heat the gas in the filament. We have shown in previous papers, based on older X-ray data, that the X-ray emission is insufficient to heat the observed warm H_2 emission over the area of the whole filament (Appleton et al. 2006; Cluver et al. 2010). However, since then, new, much deeper *Chandra* data have become available, which included 97 ks observations (O'Sullivan et al. 2009) which have sufficient depth and spatial resolution to allow a direct comparison with our [C II] and H_2 data extracted over our 18.8 × 18.8 arcsec^2 PACS apertures. The results of the X-ray temperature and abundance fits to the X-ray spectra allow us to obtain reliable X-ray luminosities over these areas (see Table 6). From these results, we can show that the [C II] to X-ray luminosity ratio, $L([C\,II])/L_{Xsoft}$, varies from 3 to 11 depending on the region. Thus, the X-ray emission is far too faint to explain both the warm H_2 and the [C II] emission, since the efficiency for heating gas by X-rays is a few percent at most. Only if the X-ray flux was underestimated significantly, could X-rays be the main heat source. This is unlikely since fits to the X-ray data do not suggest a large intervening column, nor does the observed H_2 emission seen in the IRAM observation have enough column density to provide significant X-ray obscuration. Thus, we can be confident that the X-rays are not the primary heating source for the main cooling lines.

5.3. Extended Photodissociation Regions (PDRs)?

It has been known for many years that C^+ ions can be excited in PDRs in the diffuse ISM (Tielens & Hollenbach 1985; Watson 1972; Glassgold & Langer 1974; Draine 1978; Hollenbach 1989; Bakes & Tielens 1994). The dominant mechanism is believed to be the heating of gas by photoelectric ejection of electrons from PAH molecules and small grains. The warm gas (mainly the abundant H I and H_2) would then excite [C II] emission collisionally. Various authors have provided evidence

[24] The warm molecular hydrogen is an unusually large fraction of the total gas mass. This conclusion was independently supported through the analysis of the CO emission (Guillard et al. 2012).

Table 6
X-Ray Properties of PACS Regions

PACS Region[a]	kT[b] (keV)	Z[b] (solar)	$L_{\rm Xsoft}$[b,c] (10^{33} W)	$L_{\rm Xsoft}/L_{\rm FIR}$) ($10^{33}$ W)	[C II]/$L_{\rm Xsoft}$	$H_{2tot}/L_{\rm Xsoft}$
A	0.39 ($^{+0.13}_{-0.06}$)	1.33 ($^{+1.33}_{-1.20}$)	0.90 ($^{+0.02}_{-0.02}$)	0.005	11.1 (1.7)	13.4 (0.4)
B	0.62 ($^{+0.06}_{-0.05}$)	0.12 ($^{+0.06}_{-0.04}$)	3.31 ($^{+0.25}_{-0.25}$)	0.029	2.9 (0.5)	4.6 (0.4)
C	0.71 ($^{+0.05}_{-0.09}$)	0.18 ($^{+0.09}_{-0.06}$)	3.35 ($^{+0.25}_{-0.25}$)	0.023	3.4 (0.6)	5.5 (0.4)
D	0.70 ($^{+0.07}_{-0.09}$)	0.45 ($^{+2.04}_{-0.26}$)	1.66 ($^{+0.18}_{-0.18}$)	0.012	3.6 (0.6)	6.7 (0.8)
E	0.60 ($^{+0.07}_{-0.08}$)	0.15 ($^{+0.12}_{-0.06}$)	2.19 ($^{+0.21}_{-0.21}$)	0.018	3.5 (0.6)	5.9 (0.6)

Notes.
[a] PACS regions as defined in Figure 1(b) and Table 1 covering 18.8 × 18.8 arcsec^2.
[b] Soft X-rays (0.5–2 keV) derived from extractions from the *Chandra* observations by O'Sullivan et al. (2009).
[c] Assuming $D = 94$ Mpc.

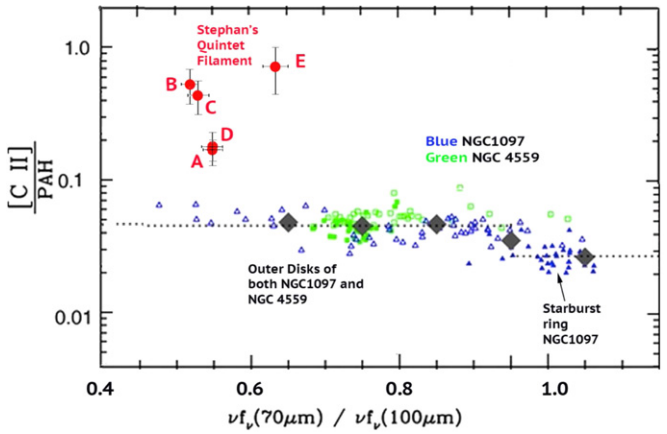

Figure 8. [C II] μm/PAH$_{\rm tot}$ ratio vs. the FIR 70/100 μm dust color for NGC 1097 and NGC 4559 from Croxall et al. (2012) KINGFISH program, with the SQ points from PACS Regions A–E plotted. The photoelectric heating efficiency in PDRs is dominated by PAH molecules, and [C II]/PAH ratio is unlikely to exceed 3% for PAHs, and a smaller amount from small and large grains according to Habart et al. (2004). The SQ points are the values PAH$_{\rm tot}$ as tabulated in Table 1, and the 70/100 μm colors are derived from the SED fits in Figure 5.

that PAHs dominate over both small and large grains in terms of photoelectric heating efficiency (Watson 1972; Hollenbach & Tielens 1999; Habart et al. 2004). The heating of the diffuse gas may be further enhanced if the metallicity of the gas is low, because UV photons can excite a larger volume at smaller net G, thereby increasing the heating efficiency (see discussion of extended PDRs by Madden et al. 1997; Israel & Maloney 2011).

One direct measure of the efficiency of photoelectric heating is the flux ratio of the [C II] to total emission from PAH features in the mid-IR spectrum [C II]/PAH$_{\rm tot}$. Here we define PAH$_{\rm tot}$ as the sum of the PAH feature fluxes from 6 to 17 μm. For diffuse regions in the Galaxy (e.g., Habart et al. 2003), this is typically few percent, and has been directly measured recently in a variety of extragalactic environments (Beirão et al. 2012; Croxall et al. 2012) ranging from 2% to 5%. Figure 8 (see also Table 1, Column 7) shows the [C II]/PAH ratio for the five PACS regions plotted against far-IR color temperature. Also shown are spatially resolved points from Croxall et al. (2012) for NGC 1097 and NGC 4559—two nearby galaxies observed in the *Herschel* KINGFISH program (Kennicutt et al. 2011). The plot emphasizes the unusually large ratios of [C II]/PAH$_{\rm tot}$ in the SQ shock compared with normal diffuse emission in the outer parts of galaxies.

Our measured values of [C II]/PAH$_{\rm tot}$ ratio range from values of 17%–18% (Regions A and D) to 40%–70% in Regions B, C, and E. The large [C II]/PAH ratios we observe, especially in Region E, strongly argue against heating of the [C II] emission by photoelectron from PAH molecules in a diffuse UV field as the primary mechanism for the [C II] emission, since the efficiency of the photoelectric effect would have to be unusually large to explain the observed result.

Cluver et al. (2010) showed that the 24 μm *Spitzer* emission from the molecular shock is very weak, perhaps even absent at the shock-center (near Region C) suggesting a dearth of small grains. This can now be quantified more precisely with the new combined *Herschel*- and *Spitzer*-derived SED (P. Guillard et al. 2013, in preparation). The 24 μm point for Region E (scaled to the 160 μm resolution—red point in lower panel of Figure 5) shows that it is extremely low, in sharp contrast to the same point in Region A known to contain some star formation (upper panel of Figure 5). Since small grains radiate most efficiently in the 20–30 μm range, it is unlikely that the [C II] emission could arise from photoelectric heating from small grains, since they seem depleted over much of the filament. Most of the emission from Region E comes from long-wavelength emission, presumably from larger grains where the photoelectric heating of [C II] is the most inefficient (Bakes & Tielens (1994).

PACS Regions B, C, and E also show unusually high [C II]/FIR ratios (Table 1). These values ([C II] between 6% and 7% of the FIR) are much larger than that seen in the diffuse ISM which is typically <1%, and exceeds by at least a factor of two the maximum theoretical efficiency for photoelectric heating of [C II] by small grains (~3%) discussed by Bakes & Tielens (1994). To put these values in a more cosmic perspective, we show in Figure 9, the [C II]/FIR ratio versus the FIR IR luminosity for the five extracted regions overlaid on a plot shown by Stacey et al. (2010) for galaxies in both the nearby and distant universe. Interestingly, the Regions A and D, where the gas filament is contaminated by star formation, show lower [C II]/FIR ratios, whereas the other regions in SQ that lie in more "pure shock" environments away from known H II regions, have higher ratios. This suggests that the signature of shocked or turbulently heated gas can be masked by star formation—perhaps explaining why such large ratios are not commonly seen in galaxies with powerful star formation.

In Figure 10, we show one regime where the observations of the SQ shock seems to fall closer to the norm seen in other galaxies. Here we plot the [O I] 63 μm/[C II] ratio as a function of the FIR dust color F (60 μm)/F (100 μm) from Malhotra et al. (2001) based on their work with *ISO* for a set or normal galaxies. Although the points lie to the extreme in color temperature (we determine these colors from the SED fits of P. Guillard et al. 2013, in preparation), the points seem to form an extension

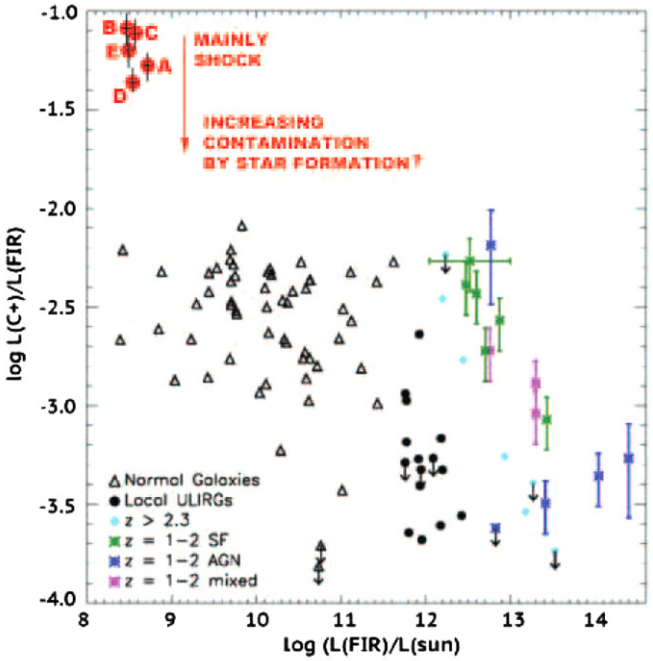

Figure 9. Compilation by Stacey et al. (2010) of the [C II]/FIR luminosity vs. the FIR luminosity for individual galaxies over a wide range of luminosity and redshift. The SQ PACS Regions A–E are also plotted showing the extreme values for the [C II]/FIR ratio, especially for the regions less contaminated by star formation (Regions B, C, and E). Interestingly, those regions exhibiting weak star formation fall closer to the distribution for normal star forming galaxies. The arrow shows a highly schematic mixing line as star formation becomes more dominant over shocks in gas that are actively forming stars rather than in a highly turbulent state.

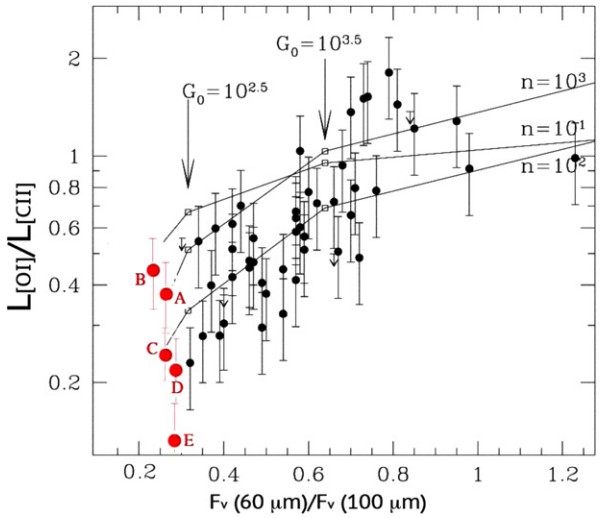

Figure 10. Line luminosity ratio of [O I]/[C II] as a function of the far-IR color from a sample of galaxies by Malhotra et al. (2001) based on *ISO* data (black points) with the PACS Regions 1–5 for SQ plotted as red filled circles. The solid lines are theoretical models of PDRs based on the models of Kaufman et al. (1999). Unlike the other figures shown in this paper, the SQ points appear to form a continuous distribution at cool color temperatures with the normal galaxies (see the text).

of those found for normal galaxies. Recent spatially resolved observations of M82 with PACS (Contursi et al. 2013) show a tail of points which also extend into this region. They mainly arise in the cooler outer parts of M82, with some points possibly being associated with the starburst wind. Malhotra et al. interpreted their plot as an indication that [O I] is excited more, with respect to C^+, as the dust temperature rises. Our results for SQ appear to confirm that this trend remains true for the gas and dust in the SQ filament, even though we have argued that the process that excites the [C II] (and presumably [O I]) is not UV radiation in a PDR. In some ways this is unfortunate, because if one is confronted with far-IR diagnostics alone, it is hard to separate shock or turbulently induced gas from a low-density PDR, since both can exist as a diffuse, warm component in the ISM.

It is interesting to ask what contribution to the [C II] emission might be expected from a standard PDR (solar abundance), given the low values of far-UV field strength G_o of 1.4 Habing units in SQ measured by Guillard et al. (2010). Such UV radiation must be present to ionize the carbon. Based on the models of Kaufman et al. (1999) and adopting a reasonable density of $\sim 10^3$ cm $^{-3}$, this low G-field would be expected to contribute a surface brightness in [C II] emission of 1–2 $\times$ 10^{-6} erg s^{-1} cm^{-2} sr $^{-1}$, or between 0.8 and 1.6 $\times$ 10^{-17} W m^{-2}, for the extraction apertures used in our PACS regions. Thus, the UV radiation field necessary to ionize carbon would contribute between 10% and 15% of the emission detected in the SQ filament regions.

Although we will argue below that the metallicity of the gas is not likely to be a large factor in explaining the results, we next consider what the consequences of reduced metallicity might be in a diffuse PDR. Israel & Maloney (2011) have detected [C II]/FIR ratios in some regions of the Large Magellanic Cloud (LMC) which range from 1% to 5% (Cloud 9 in LMC-N11 has the highest value), and several regions in the Small Magellanic Cloud (SMC) with elevated values of 0.5%–2%, still unusual compared with most galaxies. These authors argue that PDR models in low metallicity environments can just, but only just, reconcile the [C II]/FIR ratios in the LMC. The models of Bakes & Tielens (1994) can asymptotically approach values of 5% for low values of G_0. Although one could argue that in the SQ filament, even lower values of G_0 are likely, the extreme value of [C II]/FIR = 6%–7% seen in the pure-shock regions of B and E seem to push the model to the limit. When combined with the extremely large values of [C II]/PAH discussed earlier, it seems reasonable to question whether PDR heating of the gas with these large ratios is the only possible way that [C II] can be heated.

The oxygen metallicity of the gas in the SQ filament has recently been measured using optical emission lines with an IFU by Iglesias-Paramo et al. (2012). The results depend on the velocity regime being considered. Gas consistent with shock-excitation is seen in two main velocity features around 6000–6300 km s^{-1}, and around 6600 km s^{-1}. The low-velocity feature, which is broadly associated with the intruder galaxy's (NGC 7318b) velocity (and corresponding to the broad left-hand peak seen in both the [C II] and CO spectra shown in Figure 2) has close to solar metallicity, but the higher velocity gas was found to have an oxygen metallicity of 12 + log O/H = 8.35, similar to the SMC. However, this result does not agree with the earlier measurements of Xu et al. (2003) who found 12 + log(O/H) = 8.76—slightly super-solar. The differences may be due, in part, to the different methods used, but may also be due to the difficulty of measuring metallicity when the lines are broad and faint. If we accept that the higher velocity component in the [C II] and CO profiles could be of lower metallicity, how might this effect our interpretation of the global ratios, such as [C II]/PAH and [C II]/FIR? The answer is that the effect is minimal, since the average metallicity of the gas, integrated over the whole profile, is likely to be no less than 0.75 solar, especially as the lower-velocity component dominates the

integral flux of the [C II] in most of the cases shown in Figure 2. As mentioned earlier, no large differences in the $I([\mathrm{C\,II}])/I(\mathrm{CO}\ J = 1\text{–}0)$ ratio between the low- and high-velocity components are obvious, again suggesting that if the higher-velocity component in the [C II] profiles has reduced metallicity, it must also be compensated for in the CO abundance.

We note that Sargsyan et al. (2012) have noticed large [C II]/PAH ratios, particularly in galaxies with known AGN. In this case, extinction in the mid-IR was cited as a possible explanation, although no deep silicate features were observed. Furthermore, P. Guillard et al. (in preparation) have discovered similar cases in radio galaxies which already have been shown to contain shocked molecular hydrogen. Thus, although rare, galaxies with extreme [C II]/PAH ratios are beginning to emerge from the *Herschel* data. Could shock-heating, or CRs accelerated in the shock be the answer?

5.4. Cosmic-ray Heating?

We have shown that the bulk of the gas mass in the shock has to be warm ($T > 50$ K) to account for the observed high [C II] cooling rate. Since we have ruled out UV and X-ray heating, we are left with two possible heating sources of the gas. The first is CRs, and the second is the dissipation of kinetic energy through turbulence and shocks.

The SQ intergalactic filament was discovered through its synchrotron radiation in the centimeter waveband (Allen & Hartsuiker 1972; van der Hulst & Rots 1981), and thus, CRs are present in the filament. Following the same calculation done in Nesvadba et al. (2010) and Ogle et al. (2010), we compute the CR ionization rate needed to heat the observed gas mass at $T \sim 100$ K. For CRs, the heating energy per ionization is ~13 eV for H_2 gas (Glassgold et al. 2012). To heat the gas we need an ionization rate per nucleon ζ of 1 to 2.5×10^{-14} s^{-1}.

Each ionization destroys one H_2 molecule. For the gas to be molecular, the creation rate of H_2 ($\gamma_{H_2} \times n(H\,\mathrm{I}) \times n(\mathrm{H})$) should be higher than the destruction rate $\zeta \times n(H_2)$, where γ_{H2} is the H_2 formation rate coefficient. From Milky Way observations, $\gamma_{H2} \sim 1\text{–}3 \times 10^{-17}$ cm^3 s^{-1} (Jura 1975). If the molecular fraction of the gas is $f_{H2} = 2 \times n(H_2)/n(\mathrm{H})$, then the gas can be molecular if $\gamma_{H2} > \zeta \times f_{H2}/(2n(\mathrm{H}) \times (1 - f_{H2}))$. For the SQ shock, $f_{H2} > 0.95$, (based on the lack of H I detected in the filament), and so $\gamma_{H2} > 9.5 \times \zeta/n(\mathrm{H})$. For such a high molecular fraction, we would need $n(\mathrm{H}) \gg 1 \times 10^3$ cm^3 for molecules to survive if the heating comes from CRs, unless the formation rate of H_2 per collision is much larger than the Galactic value. For example, if we assume $n(\mathrm{H})$ is 1000 cm^{-3}, then γ_{H2} would be 1.9×10^{-16} cm^3 s^{-1}.[25] Therefore, we conclude that in order for CR heating to be viable, it would require much higher densities of the molecular gas than is observed.

5.5. Shocks and Turbulence as the Likely Heating Source

We believe that the most likely heating source for the gas in the filament is the dissipation of kinetic energy released through a turbulent cascade from a large scale (set by the size of the intruder galaxy and its high velocity) to a small scale, with most of the dissipation being at small scales. This heating source was proposed by Guillard et al. (2009) to account for the warm H_2 emission in SQ, and shown to be viable for the similar heating of warm H_2 in the bridge between the Taffy galaxies (Peterson et al. 2012).

There is no shortage of available energy to be dissipated in a high-velocity collision between, in this case, NGC 7318b and a pre-existing H I filament. The turbulent heating rate per unit H_2 molecule, $\Gamma_{\mathrm{turb}} = (3/2) \times 2m_{\mathrm{H}}(\sigma^2)/\tau_d$, where $\tau_d = L/\sigma$ is the dissipation timescale. Here, σ is the characteristic velocity dispersion of the gas, L is the characteristic length for the system, and m_{H} is the mass of the hydrogen atom. Given the observed velocity widths of typically $\Delta V(\mathrm{FWHM}) = 400\text{–}800$ km s^{-1}, then $\sigma = \Delta V(\mathrm{FWHM})/2.36$ for a Gaussian distribution, lies in the range 170–340 km s^{-1}. For a galaxy colliding with gas clumps with scales of order 4–8 kpc, the dissipation time is $\tau_d \sim 25$ Myr, and $\Gamma_{\mathrm{turb}} = 2\text{–}8 \times 10^{-31}$ W molecule^{-1}, or approximately 4–5 times the cooling rate of the C^+ ions ($5\text{–}8 \times 10^{-32}$ W H^{-1}—see Figure 6), and a similar magnitude for the warm H_2.

Thus, turbulence is quite capable of delivering energy at the right rate for a significant period of time. This energy is likely to be funneled to the smallest scales through a network of low-velocity shocks (Guillard et al. 2009; Lesaffre et al. 2013) or intermittent vortices (Godard et al. 2009) via supersonic turbulence. Using a similar model, B. Goddard et al. (in preparation) show that turbulent dissipation can explain unusually high [C II] emission seen in high-latitude clouds in the Galaxy, predicting a doubling of the emission compared with PDR models.

In a remarkably predictive paper, Lesaffre et al. (2013) demonstrate that even quite low velocity shocks passing through a diffuse (10^2–10^3 cm^{-3}) irradiated molecular medium can significantly boost the [C II] signal so that it becomes almost as bright as the 0–0 H_2 $S(1)$ line. These authors, who were working with previously published H_2 excitation diagrams for SQ and diffuse gas in the Chamaeleon cloud, showed that the H_2 excitation in SQ could be modeled by low-velocity C-shocks in a diffuse molecular medium. When considering mildly UV-irradiated gas (sufficient to ionize the carbon), they showed that in 7–10 km s^{-1} C-shocks, the [C II] emission can become almost as bright as the H_2 emission. In their model, 70% of the [C II] emission comes from shocked gas with only 30% from the PDR associated with the ionization of the carbon. Furthermore, these models predict weak [O I] 63 μm emission, largely because of the much lower compression of C-shocks versus more powerful J-shocks. Although their model underpredicts the ratio of [C II] to 0–0 $S(0)$ H_2 line, a network of low-velocity C-shocks is a promising direction for explaining the observations presented here.

Excluding the SQ-A star formation region, the ratio of $I([\mathrm{C\,II}])/I(\mathrm{CO}\ J = 1\text{–}0)$ is observed to lie between 1000 and 1700 in the filament. We have shown that, taken together with the high values of [C II]/FIR ratio, these values are not consistent with PDR models.

A proper model of the $I([\mathrm{C\,II}])/I(\mathrm{CO})$ ratio for the shock case is non-trivial and is highly dependent on the specific conditions, including magnetic field, density, and the treatment of the turbulent line broadening which affects the optical depth, and is beyond the scope of the present paper. The Lesaffre et al. models somewhat underpredict the $I([\mathrm{C\,II}]/I(\mathrm{CO}\ J = 1\text{–}0)$ ratios observed here, but were optimized for a different set of observational constraints.

Preliminary shock modeling, which includes post-processing with a Large Velocity Gradient (LVG) code, is able to reproduce

[25] We note that the above argument is very simplistic regarding H_2 formation, since, in reality, many complex factors affect the formation rate (e.g., Hollenbach & McKee 1979; Cazaux & Tielens 2002; Pirronello et al. 1997), and as we argue later, shocks may accelerate H_2 formation through both gas-phase and grain processes.

$I([\mathrm{C\,II}])/I(\mathrm{CO}\ J = 1\text{–}0)$ ratios of 700–3000 for pre-shock densities of 10^3 cm^{-3}. Future models of the SQ system, incorporating these kinds of models, will also have to take into account energy input to the gas from much higher velocity shocks, which Cluver et al. (2010) suggested may help to explain the relatively strong [Si II] 34.8 μm line-cooling in the filament, as well as possible cooling in important far-UV lines.

6. H_2O DETECTION: EVIDENCE FOR A DENSER WARM MOLECULAR COMPONENT AT INTERMEDIATE RADIAL VELOCITIES

The discovery of H_2O from the shock at several positions indicates that some parts of the shock must contain high densities $>10^6$ cm^{-3} and are likely the result of higher-velocity J-shocks. Furthermore, the failure to detect other lines, on either the otho- or para-water branches, is consistent with a relatively low temperature $\sim$ 80–100 K based on a simple exploration of parameter space in the RADEX models of Van der Tak et al. (2007). Such high densities are in contrast to the density needed to explain the [C II] emission, supporting the idea of the SQ filament being composed of several distinct gas phases. The line luminosity in the p-H_2O (1_{11}–0_{00}) line is 10% of the [C II] line intensity in region SSWD4 which lies close to PACS Region C and is sampled at almost the same scale. We note that in an unpublished GBT search for 22 GHz H_2O masers in the filament, none were found (P. Appleton 2012, private communication), which suggests that ultra-dense gas ($>10^7$–10^8 cm^{-3}), needed for maser action, is rare in the structure, or alternatively, that the observer is not aligned with the maser column.

As we have noted, the width of the p-H_2O line is unresolved at the FTS resolution of 324 km s^{-1} and has a heliocentric velocity in the mid-range of [C II] velocities detected in the filament. At the position of the SSWD4 footprint (see Figure 1(c)), the velocity of the line lies at 6457($\pm$90) km s^{-1}, which is between the velocity of the intruder galaxy NGC 7318b ($V =$ 5774 km s^{-1}) and the gas at the main velocity of the group ($V =$ 6600–6700 km s^{-1}). This places it at the same velocity as the majority of the warm H_2 emission (Cluver et al. 2010), and between the peaks of the CO 1–0 profile seen in the central panel of Figure 2. Thus, the H_2O line may be gas that represents the material accelerated by the intruder galaxy to intermediate velocities. Perhaps only this strongly accelerated gas is permeated by J-shocks.

It is worth discussing a very different interpretation of the line seen in the FTS spectrum of Figure 3. Could the line be identified, not with the p-H_2O line, but with ortho-H_2O^+ (1_{11}–0_{00}) which is seen in absorption in M82 (Weiß et al. 2010)? o-H_2O^+ has a transition at a rest frequency $\nu = 1115.186$ GHz (Mürtz et al. 1998), which would be blue-shifted by 507 km s^{-1} compared with p-H_2O. This would place the line at a velocity of $\sim$6000 km s^{-1}, close to the main peak in the CO and [C II] profile for Region C. A search for other H_2O^+ lines (for example the one at 1108.404 and 1132.629 GHz) yielded no detection. Nevertheless, could the detection of o-H_2O^+ be viable?

As discussed by Hollenbach et al. (2012), H_2O^+ is part of the "backbone" of interstellar chemistry in the ISM, and is a main formation route from H_2 to H_2O. In order for oH_2O^+ to be detected (without a detection of H_2O), the water would have to be very highly ionized. Models of the abundance of ionized water under various conditions of photoionization and CR ionization are presented in Figures 2 and 3 of Hollenbach et al. What is noticeable is that in almost all cases considered, the abundance of OH^+ is at least comparable, or larger than H_2O^+, especially in the more diffuse environments. These authors consider CR ionization rates of up to 2×10^{-16} s^{-1}, which is comparable to the limiting ionization cases considered in Section 5.4. At this CR ionization rate, H_2O would also be strong, and yet only one line is detected. The non-detection of the OH^+ lines at 903.684, 966.92, and 1026.903 GHz (Bekooy et al. 1985) may argue against a highly ionized medium, and the H_2O^+ interpretation of the 1113 GHz line.

7. IMPLICATIONS FOR TURBULENT GAS AT HIGH-z

The discovery of kinematically broad group-wide [C II] emission that appears too bright to be explained by star formation (either arising in H II regions or by diffuse PDRs) in Stephan's Quintet is a strong reminder that [C II] can be relatively easily enhanced by processes other than UV heating. The fact that we see the signal without strong contamination from PDR emission, as well as sharing a similar velocity space with CO (1–0) emission, suggests a close connection with the dissipation of kinetic energy in the group as the intruder crashes through the intergroup gas. The spatial extent of the observed [C II] emission covers most of the observational area of our PACS observations and undoubtably extends over the whole of the shocked filament and the bridge to NGC 7319. The large width of the [C II] line (in some places >1000 km s^{-1}) as well as its comparable power to the H_2 0–0 $S(1)$ line suggests a [C II] emission originating in a highly turbulent medium. A turbulent cascade from large-scale high-velocity shocks created in the galaxy collision, to small-scale low-velocity shocks in the H_2 gas can explain a large part of the [C II] emission.

Ogle et al. (2010) and Guillard et al. (2012) have already demonstrated that radio galaxies are often hosts of very strong warm H_2 emission and that shocks and turbulence are the main cause (see also Nesvadba et al. 2011 for additional evidence for shocks in 3C326) Furthermore, very high H_2 line luminosities have recently been found to be associated with the $z = 2$ "Spiderweb" radio galaxy (Ogle et al. 2012). Such strong emission is potentially associated with shocks within 60 kpc of the radio galaxy and surrounding satellite systems, which already shows strong filamentary Hα emission. Thus, objects like the "Spiderweb" may be scaled-up versions of the SQ phenomenon and would be ideal places to look at higher-z for enhanced [C II] emission. In this respect, it is interesting that Seymour et al. (2012) claim a possible photometric detection of [C II] in their 500 μm band at a tentative level of [C II]/FIR = 2%. Follow-up of this possible discovery with line observations would be very interesting.

Observatories like ALMA are now capable of detecting highly redshifted [C II] emission from galaxies, sometimes with higher than expected [C II]/FIR ratios (e.g., Swinbank et al. 2012). Although one explanation for the enhanced [C II] emission is that the star formation is quite extended, and the UV-field diluted, our observations of SQ provide an alternative possibility—that at least some of the extra [C II] comes from the dissipation of mechanical energy in the systems. As we illustrate in Figure 9, the regions of SQ which contain known star formation show lower values of [C II]/FIR. There is no reason to believe that SQ's filament is unique—it is simply one of the best known nearby examples of an isolated extragalactic shocked structure, quite separated from regions of strong star formation. We are currently reducing data on the Taffy bridge system, which is also known to contain a strong shock signature (Peterson et al. 2012), and preliminary indications are that the bridge also emits strong [C II] emission. It is clear from our energy dissipation discussion

in Section 5.5, that turbulence can deliver large amounts of energy to gas on a timescale comparable with star formation and should not be neglected in violently collisional situations. In an environment where dark-matter halos are scaled up (e.g., in massive radio galaxies or quasars), more energy will be available for both star formation and dissipation of mechanical energy.

Unfortunately, it is not clear how to separate the UV-heated gas from the shock-heated gas without more diagnostics than those available from a single high-z detection of [C II]. Even if [O I] is also detected, as we show in Figure 10, it is not easy to separate diffuse PDR emission from shock-induced [C II] emission, because both can lead to a diffuse, low-density medium. In addition, there is the possibility of AGN heating of the [C II], which, like higher velocity shocks, will also boost the [O I] emission. The detection of strong molecular hydrogen cooling lines in high-z galaxies, with the proposed *SPICA* telescope, or ro-vibrational lines of H_2 with *JWST*, may provide additional hope for separating PDR heating from turbulence and shocks.

8. CONCLUSIONS

We have performed the first *Herschel* observations of the giant intergalactic filament away from major regions of star formation in the compact group, Stephan's Quintet. Previous observations have provided strong evidence that the filament is the result of the supersonic collision between an intruder galaxy, NGC 7318b, and a pre-existing tidal tail in the group. Our observations with the PACS and SPIRE spectrometers lead to the following conclusions.

1. Kinematically, broad (>1000 km s^{-1}) far-IR fine-structure lines of [C II] λ157.74 μm are detected from the giant shocked filament and bridge in Stephan's Quintet. Weaker [O I] λ63.18 μm emission is also detected. The [C II] emission is very extensive, and can be decomposed into two or three different velocity components, many of which have FWHM ranging from a few hundred km s^{-1} to 733 km s^{-1}. The [C II] emission profiles at various positions in the filament are similar to CO 1–0 emission detected with IRAM in similar areas, suggesting that the molecular gas and the [C II] emission are closely related.
2. Based on a model of the heating and cooling of the [C II]- and [O I]-emitting gas, our measurements of the cooling rates in the filament suggest the emission arises in a warm diffuse medium ($90 < T < 200$ K, $10^3 < \rho < 3 \times 10^3$ cm^{-3}). The temperature and mass of the gas involved is consistent with the main collisional partner of the C^+ ion being the same warm molecular gas previously detected by *Spitzer* observations of the rotational H_2 lines, which is believed to be shock-heated.
3. The [C II] line emission exceeds by a factor of two, in most cases, the strength from the 0–0 $S(1)$ warm molecular hydrogen line, and is typically 50%–60% of the total rotational line luminosity from molecular hydrogen (0–0 $S(0)$ to 0–0 $S(5)$). In some regions [O I] 63 μm carries about the same power as the 0–0 $S(1)$ line, whereas p-H_2O is 28% of the 0–0 $S(1)$ line in the area where the SPIRE and PACS detectors overlap. Thus, the far-IR line-cooling from the giant filament is significant. Warm molecular hydrogen is still the dominant coolant over the six rotational lines detected by *Spitzer*.
4. Based on a careful comparison with previous *Spitzer* spectral mapping in the mid-IR, we find extremely large values of the ratio [C II]/PAH_{7-8}, ranging from 0.3–3, and [C II]/PAH_{total}, ranging from 0.17–0.7. Similarly, unusually large value of [C II]/FIR ranging from 0.04 to 0.07 were found in the same regions using imaging data from *Herschel* and *Spitzer* to constrain the SED. The [C II]/PAH ratios are an important measure of the heating efficiency of the diffuse ISM by photoelectric heating, and the observed values are so large that it is unlikely that most of the observed [C II] is emitted from PDRs. Furthermore, we can rule out direct UV excitation from H II regions and X-ray heating. The strong enhancement of [C II] in the filament, relative to PAH and dust continuum, suggests strong heating of the [C II] from shocks and turbulence, and not star formation.
5. Emission is also detected in several places from the p-H_2O ($1_{11}0_{00}$) line including the center of the giant filament. Unlike the [C II] and [O I] emission from that position, the H_2O emission is unresolved ($\Delta V < 360$ km s^{-1}), and has a systemic velocity placing it in the mid-range of detected [C II] emission, and at the same, velocity are strong warm H_2 detected by *Spitzer*. The detection of H_2O suggests that the SQ filament contains regions of very high gas density ($>10^6$ cm^{-3}), supporting the idea that the structure of the filament is highly multi-phase. Despite detection of the CO 1–0, 2–1, and 3–2 lines from the ground, no higher-order J lines of CO or other H_2O lines were detected with SPIRE.
6. We considered the possibility that the detected SPIRE line was H_2O^+, not H_2O, but rejected this possibility because the high ionization rates needed to completely ionize water, would also be expected to ionize OH, forming OH^+, which is not detected.
7. Models (Lesaffre et al. 2013) of mildly ($G_o \sim 1$) UV-irradiated molecular gas show that the [C II] signal can be strongly boosted without a larger increase in [O I] emission in low-velocity magnetic shocks. Although these models do not explain all the emission detected, the work strongly suggests shocks are playing a large role. In reality, the SQ filament is likely permeated by a vast network of shocks (as evidenced by the broad line-widths), including numerous low-velocity magnetic (C-) shocks traveling through molecular gas of relatively low density (100–1000 at cm^{-3})—a density which falls within the range we derive from the observations. These low-velocity shocks could be the natural consequence of turbulent energy dissipation initiated on much larger scales by the galaxy collision in the group.
8. The possibility that [C II] can be excited on a large scale by the dissipation of mechanical energy (turbulence and shocks) provides a potential new source of [C II] emission when interpreting [C II] in high-redshift galaxies (e.g., Stacey et al. 2010; Swinbank et al. 2012). Since, in this paper, there is strong evidence for a connection between the turbulent molecular gas in the SQ shocked filament, and the [C II] emission (both its distribution and kinematics), we suggest that enhanced [C II] (and warm H_2 emission) from turbulent energy dissipation should be present in most situations where highly turbulent conditions exist—such as in galaxy collisions, and in the early stages of the building of galaxy disks. However, as we have shown, the energy appears to be degraded down to very small scales and low-velocities, creating a warm diffuse gas component which is not easily distinguished from a low-density PDR. Thus, the best places to disentangle mechanically induced [C II]

emission from UV-dominated heating will be in regions where turbulent processes are present, but star formation has not yet turned on. Such conditions may exist in the early stages of galaxy formation.

P.N.A. acknowledges interesting discussions with P. Goldsmith and W. Langer (JPL) regarding [C II] emission in the Galaxy. This work is based on observations made with *Herschel*, a European Space Agency Cornerstone Mission with significant participation by NASA. Support for this work was provided by NASA through an award issued by JPL/Caltech. The authors thanks an anonymous referee for thoughtful comments on a previous version of the text.

REFERENCES

Allen, R. J., & Hartsuiker, J. W. 1972, Natur, 239, 324
Appleton, P. N., Xu, K. C., Reach, W., et al. 2006, ApJL, 639, L51
Bakes, E. L. O., & Tielens, A. G. G. M. 1994, ApJ, 427, 822
Beirão, P., Armus, L., Helou, G., et al. 2012, ApJ, 751, 144
Bekooy, J. P., Verhoeve, P., Meerts, W. L., & Dymanus, A. 1985, JChPh, 82, 3868
Casey, C. M. 2012, MNRAS, 425, 3094
Casey, C. M., Berta, S., Béthermin, M., et al. 2012, ApJ, 761, 139
Cazaux, S., & Tielens, A. G. G. M. 2002, ApJL, 575, L29
Cluver, M. E., Appleton, P. N., Boulanger, F., et al. 2010, ApJ, 710, 248
Contursi, A., Poglitsch, A., Grácia Carpio, J., et al. 2013, A&A, 549, A118
Croxall, K. V., Smith, J. D., Wolfire, M. G., et al. 2012, ApJ, 747, 81
Dale, D. A., & Helou, G. 2002, ApJ, 576, 159
Draine, B. T. 1978, ApJS, 36, 595
Draine, B. T., Roberge, W. G., & Dalgarno, A. 1983, ApJ, 264, 485
Flower, D. R., Le Bourlot, J., Pineau des Forêts, G., & Cabrit, S. 2003, MNRAS, 341, 70
Flower, D. R., & Pineau des Forêts, G. 2012, MNRAS, 421, 2786
Geng, A., Beck, A. M., Dolag, K., et al. 2012, MNRAS, 426, 3160
Glassgold, A. E., Galli, D., & Padovani, M. 2012, ApJ, 756, 157
Glassgold, A. E., & Langer, W. D. 1974, ApJ, 193, 73
Godard, B., Falgarone, E., & Pineau Des Forêts, G. 2009, A&A, 495, 847
González-Alfonso, E., Fischer, J., Graciá-Carpio, J., et al. 2012, A&A, 541, A4
Griffin, M. J., Abergel, A., Abreu, A., et al. 2010, A&A, 518, L3
Guillard, P., Boulanger, F., Cluver, M. E., et al. 2010, A&A, 518, A59
Guillard, P., Boulanger, F., Pineau Des Forêts, G., & Appleton, P. N. 2009, A&A, 502, 515
Guillard, P., Boulanger, F., Pineau Des Forêts, G., et al. 2012, ApJ, 749, 158
Habart, E., Boulanger, F., Verstraete, L., et al. 2003, A&A, 397, 623
Habart, E., Natta, A., & Krügel, E. 2004, A&A, 427, 179
Helou, G., Soifer, B. T., & Rowan-Robinson, M. 1985, ApJL, 298, L7
Hollenbach, D., Kaufman, M. J., Neufeld, D., Wolfire, M., & Goicoechea, J. R. 2012, ApJ, 754, 105
Hollenbach, D., & McKee, C. F. 1979, ApJS, 41, 555
Hollenbach, D., & McKee, C. F. 1989, ApJ, 342, 306
Hollenbach, D. J. 1989, in IAU Symp. 135, Interstellar Dust, ed. L.J. Allamandola & A.G.G.M. Tielens (Cambridge: Cambridge Univ. Press), 227
Hollenbach, D. J., & Tielens, A. G. G. M. 1999, RvMP, 71, 173
Hwang, J.-S., Struck, C., Renaud, F., & Appleton, P. N. 2012, MNRAS, 419, 1780
Iglesias-Paramo, J., Lopez-Martin, L., Vilchez, J. M., Petropoulou, V., & Sulentic, J. W. 2012, A&A, 539, 127
Israel, F. P., & Maloney, P. R. 2011, A&A, 531, A19
Jura, M. 1975, ApJ, 197, 581
Kaufman, M. J., Wolfire, M. G., Hollenbach, D. J., & Luhman, M. L. 1999, ApJ, 527, 795
Kennicutt, R. C., Calzetti, D., Aniano, G., et al. 2011, PASP, 123, 1347
Lesaffre, P., Pineau Des Forêts, G., Godard, B., et al. 2013, A&A, 550, A106
Madden, S. C., Poglitsch, A., Geis, N., Stacey, G. J., & Townes, C. H. 1997, ApJ, 483, 200
Malhotra, S., Kaufman, M. J., Hollenbach, D., et al. 2001, ApJ, 561, 766
Moles, M., Marquez, I., & Sulentic, J. W. 1998, A&A, 334, 473
Mürtz, P., Zink, L. R., Evenson, K. M., & Brown, J. M. 1998, JChPh, 109, 9744
Natale, G., Tuffs, R. J., Xu, C. K., et al. 2010, ApJ, 725, 955
Nesvadba, N. P. H., Boulanger, F., Lehnert, M. D., Guillard, P., & Salome, P. 2011, A&A, 536, L5
Nesvadba, N. P. H., Boulanger, F., Salomé, P., et al. 2010, A&A, 521, A65
Oberst, T. E., Parshley, S. C., Stacey, G. J., et al. 2006, ApJL, 652, L125
Ogle, P., Boulanger, F., Guillard, P., et al. 2010, ApJ, 724, 1193
Ogle, P., Davies, J. E., Appleton, P. N., et al. 2012, ApJ, 751, 13
O'Sullivan, E., Giacintucci, S., Vrtilek, J. M., Raychaudhury, S., & David, L. P. 2009, ApJ, 701, 1560
Ott, S. 2010, in ASP Conf. Ser. 434, Astronomical Data Analysis Software and Systems XIX, ed. Y. Mizumoto, K.-I. Morita, & M. Ohishi (San Francisco, CA: ASP), 139
Peterson, B. W., Appleton, P. N., Helou, G., et al. 2012, ApJ, 751, 11
Pilbratt, G. L., Riedinger, J. R., Passvogel, T., et al. 2010, A&A, 518, L1
Pirronello, V., Liu, C., Shen, L., & Vidali, G. 1997, ApJL, 475, L69
Poglitsch, A., Waelkens, C., Geis, N., et al. 2010, A&A, 518, L2
Renaud, F., Appleton, P. N., & Xu, C. K. 2010, ApJ, 724, 80
Roussel, H., Helou, G., Hollenbach, D. J., et al. 2007, ApJ, 669, 959
Sargsyan, L., Gevorgyan, M., Abrahamyan, H. V., et al. 2012, Ap, 55, 460
Seymour, N., Altieri, B., De Breuck, C., et al. 2012, ApJ, 755, 146
Smith, J. D. T., Armus, L., Dale, D. A., et al. 2007a, PASP, 119, 1133
Smith, J. D. T., Draine, B. T., Dale, D. A., et al. 2007b, ApJ, 656, 770
Smith, R. K., Brickhouse, N. S., Liedahl, D. A., & Raymond, J. C. 2001, ApJL, 556, L91
Stacey, G. J., Geis, N., Genzel, R., et al. 1991, ApJ, 373, 423
Stacey, G. J., Hailey-Dunsheath, S., Ferkinhoff, C., et al. 2010, ApJ, 724, 957
Sturm, E., Bauer, O. H., Brauer, J., et al. 1998, in ASP Conf. Ser. 145, Astronomical Data Analysis Software and Systems VII, ed. R. Albrecht, R. N. Hook, & H. A. Bushouse (San Francisco, CA: ASP), 161
Sulentic, J. W., Rosado, M., Dultzin-Hacyan, D., et al. 2001, AJ, 122, 2993
Suzuki, T., Kaneda, H., Onaka, T., & Kitayama, T. 2011, ApJL, 731, L12
Swinbank, A. M., Karim, A., Smail, I., et al. 2012, MNRAS, 427, 1066
Tielens, A. G. G. M., & Hollenbach, D. 1985, ApJ, 291, 722
Trancho, G., Konstantopoulos, I. S., Bastian, N., et al. 2012, ApJ, 748, 102
Trinchieri, G., Sulentic, J., Pietsch, W., & Breitschwerdt, D. 2005, A&A, 444, 697
van der Hulst, J. M., & Rots, A. H. 1981, AJ, 86, 1775
Van der Tak, F. F. S., Black, J. H., Schoier, F. L., Jansen, D. J., & van Dishoeck, E. F. 2007, A&A, 468, 627
Watson, W. D. 1972, ApJ, 176, 103
Weiß, A., Requena-Torres, M. A., Güsten, R., et al. 2010, A&A, 521, L1
Williams, B. A., Yun, M. S., & Verdes-Montenegro, L. 2002, AJ, 123, 2417
Xu, C. K., Iglesias-Páramo, J., Burgarella, D., et al. 2005, ApJL, 619, L95
Xu, C. K., Lu, N., Condon, J. J., Dopita, M., & Tuffs, R. J. 2003, ApJ, 595, 665